Department of Physics and Astronomy

University of Heidelberg

Master thesis

in Physics

submitted by

Christian Graf

born in Warburg

February 2015

A Calibration Scheme for the Mu3e Tile Detector

This Master thesis has been carried out by Christian Graf

at the

Kirchhoff Institute for Physics

under the supervision of

Prof. Dr. Hans-Christian Schultz-Coulon

Abstract

The standard model of particle physics (SM) successfully describes most fundamental properties and interactions of elementary particles. Nevertheless it has well-known shortcomings. This leads to theories extending the SM, some of which predict a concept called lepton flavor violation in the charged lepton sector, which has never been observed. One experiment searching for lepton flavor violation in the charged lepton sector is the Mu3e experiment. It aims at measuring the lepton flavor violating decay $\mu^+ \to e^+ e^+ e^-$ with a sensitivity of 1 in 10^{-16} decays. To achieve this goal, a precise time resolution of $100\,\mathrm{ps}$ is essential and will be provided by the Mu3e tile detector.

This thesis presents a scheme for the time calibration of the Mu3e tile detector. Several processes are analyzed regarding their feasibility in the calibration process. It is shown that the stations of the tile detector can be calibrated by using particles which produce multiple hits in different tiles. An uncertainty on the calibration of less than $20\,\mathrm{ps}$ is achieved in less than a second of simulated data. Furthermore, suggestions are given for the reduction of systematic uncertainties and the calibration of different stations with each other. In this context, a procedure for assigning a time-stamp to a reconstructed particle track is developed. An efficiency of $99.5\,\%$ is achieved for decay rates as expected in the first phase of the experiment and $93.7\,\%$ for the high rate phase.

Zusammenfassung

Das Standard Modell der Teilchenphysik (SM) beschreibt erfolgreich die meisten fundamentalen Eigenschaften und Wechselwirkungen von Elementarteilchen. Trotzdem hat es bekannte Defizite. Deshalb werden Theorien entwickelt die das SM erweitern. Manche dieser erweiterten Theorien sagen das Konzept der Leptonenzahlverletzung für geladene Leptonen vorher, welches allerdings bisher noch nicht beobachtet wurde. Eines der Experimente die nach Leptonenzahlverletzung für geladene Leptonen suchen ist das Mu3e Experiment, mit dem Ziel den Leptonenzahl verletzenden Zerfall $\mu^+ \to e^+ e^+ e^-$ mit einer Sensitivität von 1 in 10^{-16} zu messen. Um dies zu erreichen wird unter anderem eine Zeitauflösung von $100\,\mathrm{ps}$ benötigt. Diese wird durch den Mu3e Kacheldetektor erreicht werden.

Diese Arbeit prsäentiert einen Vorschlag zur Zeitkalibration des Mu3e Kacheldetektors. Verschiedene Prozesse werden hinsichtlich ihrer Gebrauchstauglichkeit für die Kalibration hin untersucht. Es wird gezeigt, dass eine Station durch Teilchen kalibriert werden kann, die in mehreren Kacheln ein Signal erzeugen. Hierdurch konnte eine Station des Detektors unter der Verwendung von weniger als einer Sekunde von simulierten Daten auf eine Genauigkeit von unter $20\,\mathrm{ps}$ kalibriert werden. Desweiteren werden Vorschläge diskutiert wie die verschiedenen Stationen untereinander kalibriert werden können. In diesem Kontext wurde ein Verfahren für die Zuweisung von Zeitstempeln aus dem Kacheldetektor an die Zugehörigen rekonstruierten Teilchenspuren entwickelt. Es wird eine Effizienz von $99.5\,\%$ für Zerfallsraten erreicht, wie sie in der ersten Phase des Experiments erwartet werden. Für die zehnfache Rate wird eine Effizienz von $93.7\,\%$ erziehlt.

Contents

Acronyms

SM standard model of particle physics

BSM beyond the standard model

PSI Paul-Scherrer-Institute

LHC Large Hadron Collider

SUSY supersymmetry

LFV lepton flavor violation

HV-MAPS high-voltage monolithic active pixel sensor

SiPM silicon photomultiplier

PMT photomultiplier tube

APD avalanche photodiode

MS multiple scattering

IC internal conversion decay

TOF time of flight

TOT time over threshold

ASIC application specific integrated circuit

TDC time to digital converter

HV high voltage

FPGA field-programmable gate array

DAQ data acquisition

CC coarse counter

GPU graphics processing unit

EAS extensive air showers

Introduction

In particle physics, the elementary questions of the underlying laws of nature are addressed. It is the study of the properties and interactions of the most fundamental particles. Although there is a consistent model of those particles, that successfully describes elementary processes with high precision, known as the *standard model of particle physics (SM)*, we know that the model is not yet complete. Thus, new ways have to be found to extend the SM, and to develop and verify new theories.

In particle physics, theory and experiment are in an especially close relationship. On the one hand, new theories make predictions that can be confirmed or rejected by experiments. On the other hand, experiments might discover new effects that give rise to new theories. The experimental side has two main approaches: First, the high energy frontier aims at discovering new particles, or processes at high energetic particle collisions, like at the Large Hadron Collider (LHC). Secondly, there are precision measurements, that measure fundamental constants or processes and try to confirm the SM, or to discover tiny differences between experiment and theory. A subgroup of precision measurements are high rate experiments that intend to measure rare processes at very high particle rates.

The *Mu3e experiment* is such a high rate experiment. It will be located at the Paul-Scherrer-Institute (PSI) in Switzerland. The experiment aims at measuring or excluding the decay $\mu^+ \to e^+e^+e^-$ with a sensitivity of 1 in 10^{16}. Despite this decay has never been seen before, it is predicted by many theories that extend the SM. While an observation of that decay would directly imply new physics, an exclusion of the decay would set limits on the parameters of theories extending the SM. To achieve the proposed sensitivity, a rate of more than a billion muon decays per second will be observed.

The Mu3e experiment is organized in three sub-detectors, one of which is the *Mu3e tile detector*. The tile detector is a timing detector providing a time resolution of less than $100\,\mathrm{ps}$ on the arrival time of particles, which is necessary to reduce the combinatorial background. The tile detector consists of a few thousand scintillating tiles, each about half a centimeter in size and made out of a scintillator material. A particle traveling through these tiles produces light by the scintillation mechanism. A silicon photomultiplier (SiPM), a light detection device, is placed underneath each tile to measure the light produced by the particles. The corresponding read-out electronics then generate precise time-stamps.

However, the time-stamps refer to the time, when the signals are processed by the read-out electronics and not to the arrival time of the particles in the tile detector. Because of differences in cable length between the tiles, or differences in the channel response of the electronics, there may be a delay between the processing of those signals between different tiles. To account for that and to reach the proposed time resolution, a relative time calibration between the tiles has to be performed.

This thesis investigates possibilities of a calibration of the Mu3e tile detector and provides a calibration scheme. Furthermore, tools and studies necessary for a calibration are presented. The development of these tools is performed by using an existing detector simulation.

The thesis is organized in two main parts. The introductory part provides background information about the theoretical motivation (chapter 1), an overview of the Mu3e experiment (chapter 2) and a more detailed description of the design and the components of the Mu3e tile detector (chapter 3). The second part begins with a brief description of the simulation procedure and an overview of the data sets used within the scope of this thesis (chapter 4), followed by a collection of preliminary studies necessary for the calibration (chapter 5). In chapter 6, a procedure is presented that assigns a time-stamp of the tile detector to the corresponding track of a particle, which marks an important part of the full event reconstruction. Finally, a scheme for the time calibration of the Mu3e tile detector is proposed in chapter 7. In this context, studies are done to investigate the possibility of various tools for the calibration and a detailed procedure is presented for a full calibration of a station of the tile detector. Furthermore, suggestions are given for a calibration between different stations.

Part I.

Theory and Concept of the Mu3e Experiment

1. Theoretical Background

This section gives a brief introduction to the theoretical concepts relevant for this thesis. This includes an overview of the standard model of particle physics, the standard model decay of the muon, and basic information about lepton flavor violation, which is a key motivation for the Mu3e experiment.

1.1. The Standard Model of Particle Physics and Beyond

The recent discovery of a higgs boson [1, 2] proves once again the importance and huge success of the standard model of particle physics (SM). The SM based on quantum fields. It describes the fundamental particles as excitations of those fields and the interaction of the particles with each other. The particle content of the SM is shown in fig. 1.1. All particles are subdivided into fermions and bosons, where both types can be distinguished by their spin, an intrinsic property of particles. While elementary fermions have a spin of $1/2$, bosons have an integer spin.

The SM contains twelve fermions: six quarks and six leptons, for which also the corresponding anti-particles exist. Anti-particles are identical to their counterpart except for an opposite signed charge; for example, the positron is the positively charged anti-particle of the electron.[1] Leptons are further organized in two types: The charged leptons (e, μ, τ) and the corresponding charge- and massless neutrinos $(\nu_e, \nu_\mu, \nu_\tau)$; or in three generations: First generation (e, ν_e), second generation (μ, ν_μ) and third generation (τ, ν_τ).

The gauge bosons are the mediators of the strong, electromagnetic and weak force. Gluons are the exchange particles of the strong force and only couple to quarks. Photons mediate the electromagentic force and couple to quarks and charged leptons and the W- and Z-bosons transfer the weak interaction, which couples to all fermions in the SM. The higgs boson completes the particle content of the SM. It is an excitation of the higgs field, which generates the mass of all particles.

The SM is very successful in predicting and calculating particle interactions with high precision.

---

[1] For simplicity, throughout this thesis, anti-particles may generically be named by their particle partner. For example, the term electron refers to both electrons and positrons, if not stated otherwise.

Within the SM, a number of particles were predicted by theory first — e.g., the Z boson [3], the top and bottom quark [4], or, the higgs boson [5, 6] — and successfully discovered later [7, 8].

Nevertheless, there are issues in particle physics which cannot, or are not likely to be explained by the SM. Examples include the nature of dark matter, which is believed to represent up to 85 % of the matter content in our universe; the relativley low mass of the higgs boson, called fine-tuning of the higgs mass, or the reason why there are exactly three generations of fermions. Those deficits drive physicists to extend the SM with theories summarized as beyond the standard model (BSM). There is a huge variety of BSM models. Example are: supersymmetry (SUSY) models, models with extra dimensions, extensions of the higgs-sector, or models introducing an additional heavy gauge boson (e.g., Z'-models) [9].

Many BSM searches focus on properties of the second generation charged lepton, the muon. As such, it is of special interest for this thesis and will be introduced in more detail in the following.
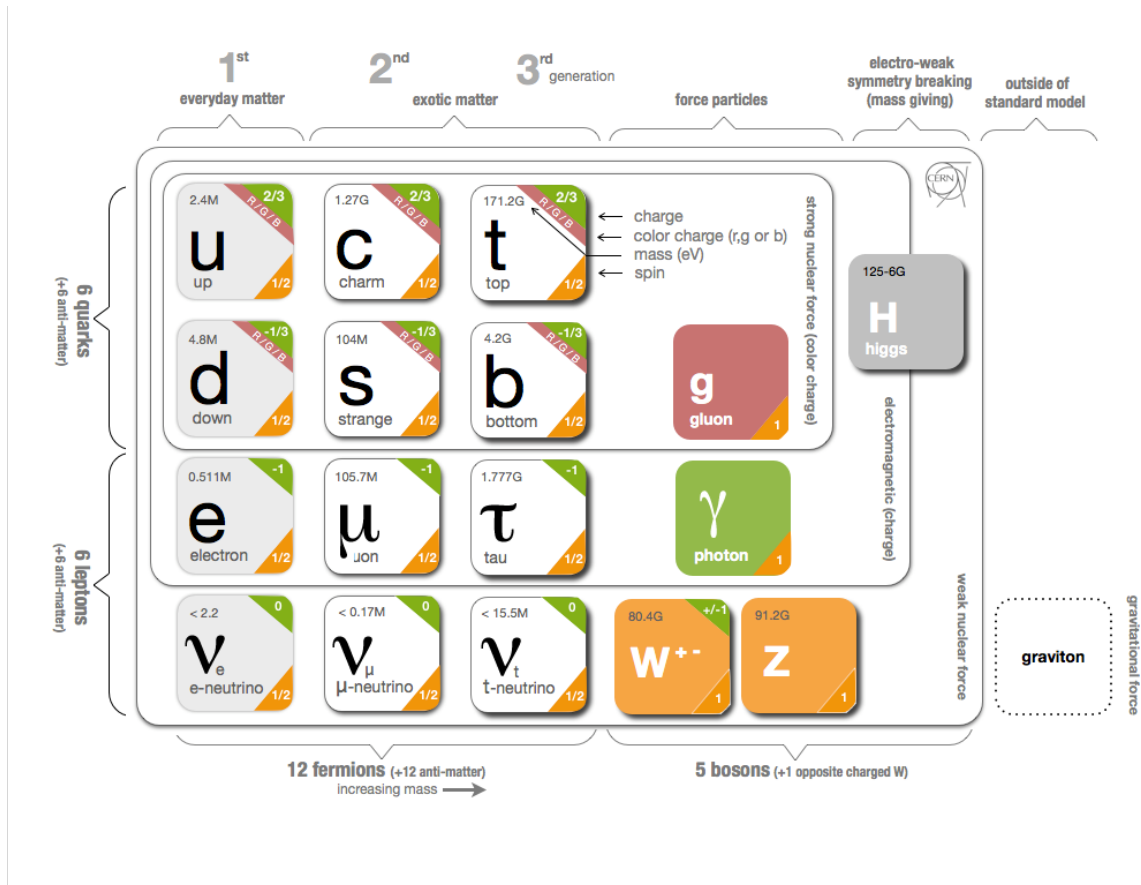

Figure 1.1.: Overview of the particle content in the standard model of particle physics. [10]

1.2. The Muon

The muon is the second generation partner of the electron. With a mass of $m_\mu = 105.7\,\text{MeV}$ [11], it is about 200 times heavier than the electron ($m_e = 511.0\,\text{keV}$ [12]). While the electron is stable, the muon decays with a mean lifetime of $2.2\,\mu\text{s}$ [11].

Decay of the (Anti-)Muon

Figure 1.2a shows the dominant decay of an anti-muon into a positron and two neutrinos, called *Michel decay*. The Michel decay is a three-body-decay. Because of energy and momentum conservation, the kinetic energy of the produced electron in the rest frame of the muon has a sharp maximum at half the muon mass (see fig. 1.3a). The Michel decay is realized via the weak interaction. A special feature of the weak interaction mediated by W-bosons is, that it only couples on chiral left-handed particles and chiral right-handed anti-particles. For massless particles, chirality is the same as helicity, which is the direction of the spin relative to the momentum of a particle. For a left-handed particle, the spin and momentum are anti-parallel, for a right-handed particle, the spin and momentum are parallel. If the primary muon is polarized, meaning its spin points in a certain direction, the Michel spectrum depends on the angle between the muon polarization and the electron momentum (see fig. 1.3b). Electrons with an energy from the right, i.e. higher energy, end of the Michel spectrum are more likely to have a momentum in the opposite direction to the spin of the muon.

The muon can also decay with the additional production of an e^+e^- pair with a branching ratio of 3.4×10^{-5} [11]. Those decays are called *internal conversion decays (ICs)* and the corresponding Feynman diagram is shown in fig. 1.2b.

More interesting decays of the muon can be realized by BSM physics. They require the idea of lepton flavor violation, which is not supported in the SM and will be introduced in the following section.
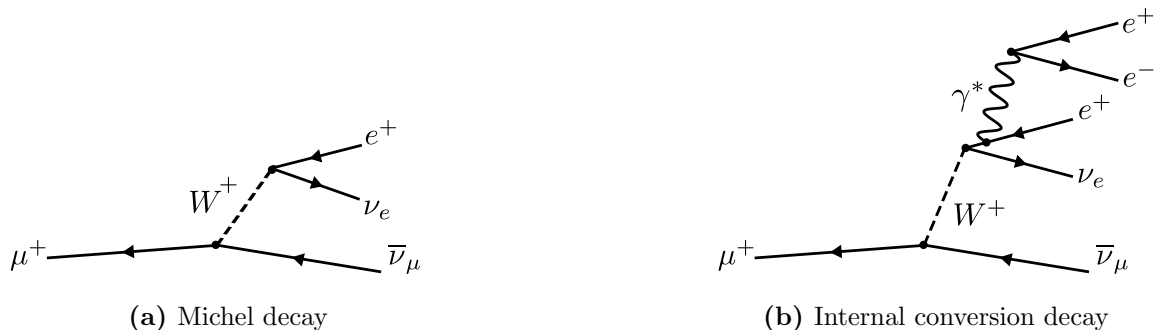

(a) Michel decay   **(b)** Internal conversion decay

Figure 1.2.: Feynman diagram of **(a)** a Michel decay and **(b)** an internal conversion decay [13].

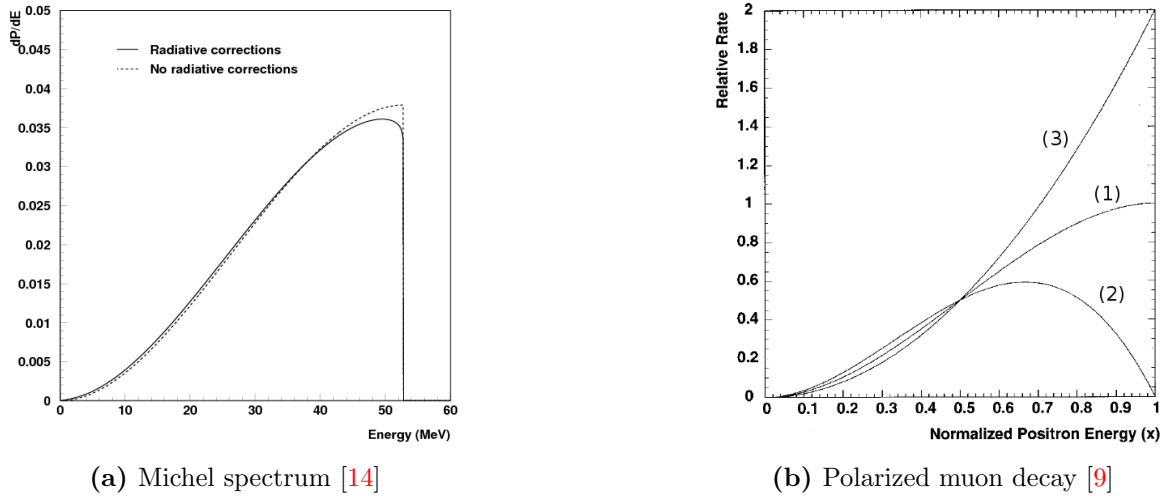**(a)** Michel spectrum [14]   **(b)** Polarized muon decay [9]

Figure 1.3.: (a) Michel spectrum: Energy distribution of the electron produced by muon decaying at rest. The dashed line shows the spectrum without radiative corrections.**(b)** Rate spectrum of positron energy in the decay $\mu^+ \to e^+ \nu_e \bar{\nu}_\mu$ of polarized anti-muons for three different angles θ_e between the muon polarization and the positron momentum. **(1)** $\cos\theta_e = 0$; **(2)** $\cos\theta_e = 1$; **(3)** $\cos\theta_e = -1$.

1.3. Lepton Flavor Violation and the decay $\mu \to eee$

The SM contains the concept of the conservation of the individual lepton numbers. The lepton numbers L_e, L_μ, and L_τ are defined for each generation. While particles have a positive lepton number (e.g., electron: $L_e = 1$), anti-particles carry a negative lepton number (e.g., positron: $L_e = -1$).

Nevertheless, violations of this conservation law (called *lepton flavor violation (LFV)*) were already observed in the neutrino sector by various experiments like SNO, Double Chooze, or T2K [15]. This effect is known as *neutrino oscillation*. For example, an electron neutrino ν_e ($L_e = 1$, $L_\mu = 0$) may oscillate into a muon neutrino ν_μ ($L_e = 0$, $L_\mu = 1$). To account for this effect, the SM is extended by introducing neutrino masses that explain the neutrino oscillation. However, despite many searches, LFV was never observed in the charged lepton sector. One possibility of LFV in the charged lepton sector is the decay of a muon into three electrons $\mu^+ \to e^+ e^+ e^-$ (in the following referred to as $\mu \to eee$). As shown in fig. 1.4a, this decay may be realized with neutrino oscillation. Yet, the decay via neutrino oscillation is suppressed by a factor of [16]

$$\text{BR}(\mu \to eee; \text{SM}) \propto \left(\frac{(m_{\nu,\mu} - m_{\nu,e})^2}{m_W^2} \right)^2 \ll 1 \times 10^{-50}, \tag{1.1}$$

and thus not observable. Here, $m_{\nu,\mu}$ and $m_{\nu,e}$ are the muon and electron neutrino mass, and m_W is the mass of the W-boson. Because of this suppression, any observation of the $\mu \to eee$ decay would directly imply new physics beyond the standard model.

Many BSM models like SUSY, Z'-models, or leptoquark models predict LFV in the charged

lepton sector [9]. A special feature of the decay $\mu \to eee$ is, that it can test for two different kind of diagrams: Loop diagrams as shown in fig. 1.4b, or direct tree diagrams (fig. 1.4c).

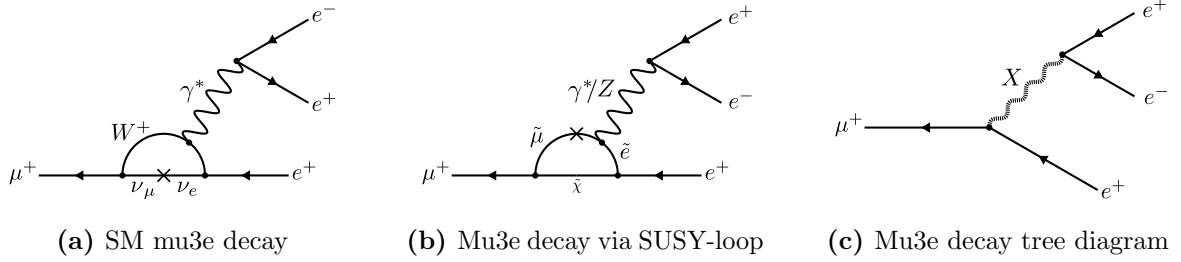**(a)** SM mu3e decay   **(b)** Mu3e decay via SUSY-loop   **(c)** Mu3e decay tree diagram

Figure 1.4.: Feynman graph of three decays of a muon in three electrons. **(a)** The suppressed SM decay via neutrino oscillation, **(b)** Loop diagram via lepton flavor violating SUSY particles, and (c) tree diagram via a hypothetical lepton flavor violating particle X [13].

2. The Mu3e Experiment

The Mu3e experiment aims to measure the LFV decay $\mu \to eee$, with a sensitivity of 10^{-16}. The experiment will be located at Paul-Scherrer-Institute (PSI), Switzerland. A research proposal can be found at [17]. In the following, an overview of the detector principle is given.

2.1. Motivation

Experiments at the low energy scale are highly complementary to high energy physics experiments like the ones at the Large Hadron Collider (LHC). While the latter are more suitable to produce and measure new particles on shell but are often suffering from high background, low and mid energy precision measurements allow to test for new physics at scales even beyond the reach of the LHC via loop contributions. LFV searches have a long history (see fig. 2.1). The most stringent limit on LFV models is currently set by the MEG-collaboration [18] at PSI excluding the decay $\mu \to e\gamma$ at $B(\mu \to e\gamma) < 2.4 \times 10^{-12}$ [19]. Other studies are for example performed by Belle and BaBar searching for forbidden tau decays (e.g., $\tau \to \mu\gamma$ or $\tau \to \mu\mu\mu$) [20, 21] or SINDRUM II investigating the muon-electron conversion $\mu\text{Au} \to e\text{Au}$ [22]. The current limit on the $\mu \to eee$ branching ratio is $B(\mu \to eee) < 1 \times 10^{-12}$ measured by the SINDRUM experiment at PSI [23]. Pushing this limit by the proposed four orders of magnitude to 10^{-16} will be a major advance in this highly interesting field of LFV physics.
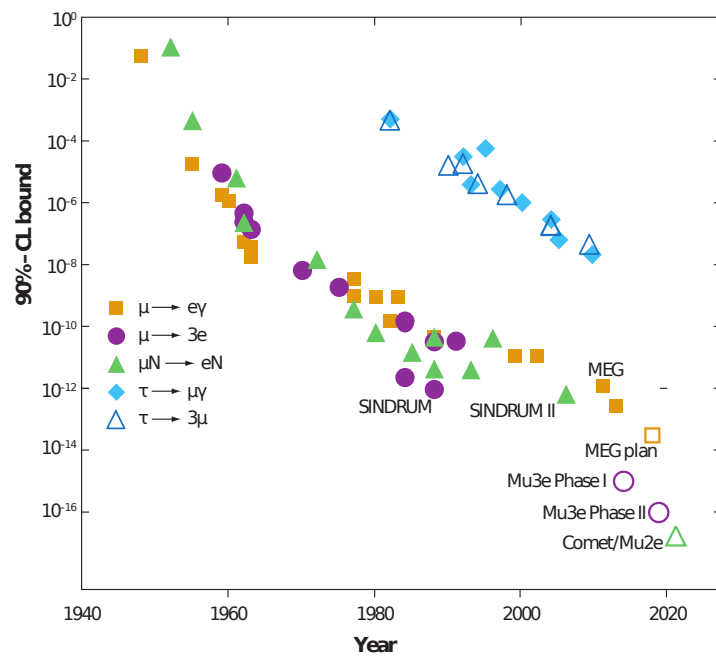
Figure 2.1.: History of searches for LFV. Shown are the 90 % confidence level exclusion limits. Also marked are the expected Mu3e limits. [24]

2.2. Signal and Background

A possible decay topology of the signal $\mu^+ \to e^+ e^+ e^-$ is shown in fig. 2.2a. It is characterized by two electrons and one positron produced at a single common vertex without any neutrinos produced. Because of energy and momentum conservation, the sum of the momentum of all three decay products has to vanish in the rest frame of the muon (which is approximately the lab frame, because the muons decay at rest):

$$|\vec{p}_{tot}| = \left|\sum \vec{p}_i\right| = 0. \tag{2.1}$$

Furthermore, the total energy has to add up to the muon mass:

$$E_{tot} = \sum E_i = m_\mu. \tag{2.2}$$

There are two different types of background. Their decay topologies are compared with the signal in fig. 2.2. The first type of background is the irreducible background caused by *internal conversion decays* ($\mu^+ \to e^+ e^+ e^- \nu_e \bar{\nu}_\mu$, see section 1.2). It can be distinguished from the signal by the additional produced neutrinos. For this purpose, a good momentum resolution is needed to verify eq. (2.1) and eq. (2.2). The second type is the accidental background. Many processes are contributing to this, but it is dominated by an overlay of a Michel decay ($\mu^+ \to e^+ \nu_e \bar{\nu}_\mu$) and bhabha scattering ($e^+ e^- \to e^+ e^-$) of a positron and an electron in the target (fig. 2.2c). To reduce the accidental background the different processes have to be separated in space and time by a good vertex and time resolution.
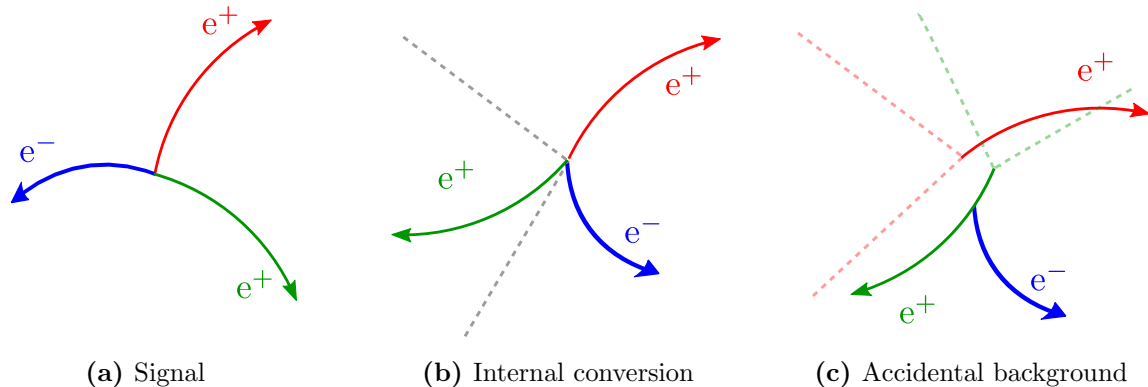

(a) Signal   **(b)** Internal conversion   **(c)** Accidental background

Figure 2.2.: Comparison of the decay topologies of signal and background events. For the signal **(a)** all three decay products are produced at the same point in space and time (vertex). The sum over the energy of them adds up to the muon mass. The internal conversion decay **(b)** produces two additional neutrinos leading to missing energy in the detector. The most dominant accidental background is shown in **(c)** an overlay of a pure Michel decay (red) and a positron (green) doing Bhabha scattering with an electron from the target (blue). This can be distinguished from the signal by the different origin of the decay products in space and time.

2.3. The Detector

To measure the decay $\mu \to eee$ with a sensitivity of up to 10^{-16}, a high intensity and low energy muon beam is required. This will be provided by PSI. The muons are stopped at a very thin double cone target made of a special aluminum foil with a thickness of 30 nm at the front and 80 nm at the back.

The momentum resolution will be achieved by a silicon pixel tracker in a magnetic field. The particle's track is reconstructed by several layers of active pixel sensors. The momentum p of the particle can then be determined by the radius R of the track ($p \propto R$). Because the electrons from a muon decay at rest have relatively low momentum, multiple scattering (MS) in the detector dominates the resolution. Thus, the main issue during the detector design is to reduce the material budget in order to minimize MS. To fulfill this requirement, the silicon pixel detector will be composed of high-voltage monolithic active pixel sensors (HV-MAPSs) [25], that can be thinned down to a thickness of approximately 50 µm.

The detector setup is modular and organized in three phases. An overview of the proposed detector and the different phases is shown in fig. 2.3. Figure 2.4 shows a cross-section through the middle of the whole detector.

The Phase Ia detector (fig. 2.3a) will run with a minimal configuration, containing only four layers of the silicon pixel tracker in the central station. It is intended to run at a rate of about 1×10^7 decays/s and its momentum resolution will be sufficient to achieve a sensitivity of $\mathcal{O}(10^{-14})$. The accidental background will be reduced only by vertex reconstruction.

For Phase Ib (fig. 2.3b), a fiber detector is added between layer 2 and 3 of the pixel detector. Furthermore, two recurl stations with two additional layers of the silicon pixel detector and a tile detector on the up- and downstream side of the central station are added. The additional pixel layers will enhance the momentum resolution of the detector significantly due to the large lever arm. The fiber detector in the central station consists of three layers of scintillating fibers with a diameter of 250 µm. Its light will be detected with SiPMs, which are placed directly underneath the tiles. The expected time resolution of the fiber detector is less than 1 ns. The time resolution of the recurl stations is even better (less than 100 ps). Due to the less stringent material budget in the recurl stations, the scintillating tiles are much thicker than the fibers which leads to more light output and thus the better time resolution. The tile detector will be discussed in detail in chapter 3. The Phase Ib experiment can run at the full muon rate of the compact muon beam line at PSI of about 10^8 decays/s.

The proposed sensitivity of $\mathcal{O}(10^{-16})$ on the $\mu \to eee$ decay will be achieved in phase 2 of the experiment. To reach this sensitivity within a reasonable measurement time of a few years (10^7 s), a high intensity muon beam with 10^9 decays/s is needed. This is planned to be realized with a possible new beam-line at PSI. To completely exploit the high rate, two more recurl stations will be added. The downside of the higher rate is an increase in pile-up, which will be discussed in section 5.2.
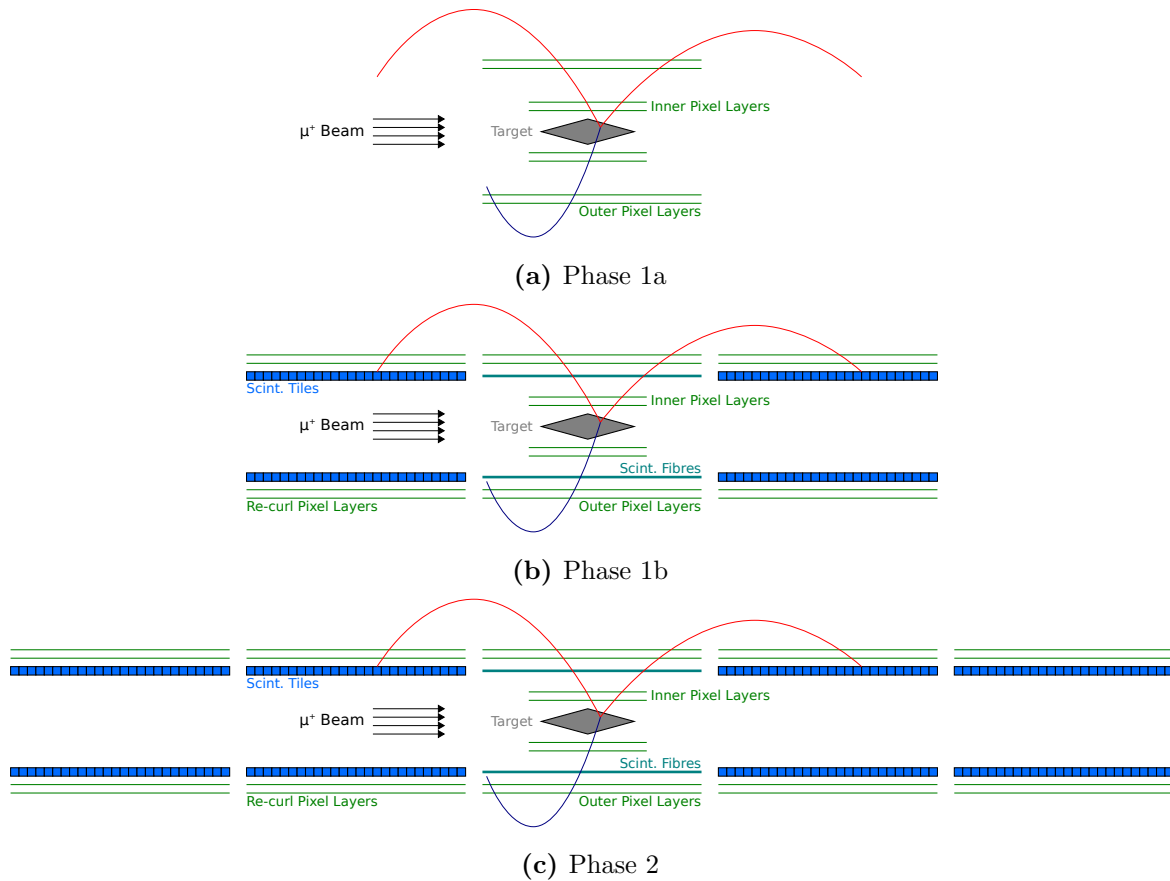
(a) Phase 1a

(b) Phase 1b

(c) Phase 2

Figure 2.3.: The detector for the different phases of the Mu3e experiment. For all three phases the muons decay on a double cone target in the center of the detector. **(a)** Phase 1a will be a minimal configuration of only four layers of the silicon pixel tracker. **(b)** In phase 1b, the fiber detector as well as two recurl stations with additional layers of the pixel tracker and the tile detector are added. **(c)** The final configuration in phase 2 includes two more recurl stations and will be operated at a different beam line with a higher muon rate. (Adapted from [17] and [13])
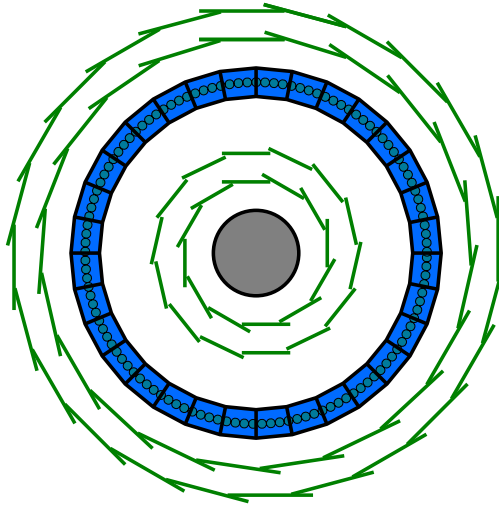
Figure 2.4.: Cross section through the detector perpendicular to the beam line for phase 1b and phase 2. The double cone target is shown in the middle, followed by the first two pixel layers surrounding the target. At larger radii are the tiles and fiber detectors, which are superimposed in this drawing, and the two outer pixel layers. It can be seen that the pixel layers are overlapping to increase the acceptance. (Adapted from [17] and [13])

2.4. Data Acquisition

The Mu3e detector is designed to operate without a hardware trigger. The read-out boards of the sub-detectors are continuously sending information to a filter farm in a way that every processing unit is given the complete detector information for a certain time frame. The filter farm runs graphics processing units (GPUs) that are performing a parallel, full online reconstruction for all events [17]. Thus, the reconstruction has to be fast and has to be able to be highly parallelized.

2.5. Simulation & Reconstruction

A full detector simulation based on the Geant4 simulation toolkit [26] is available (see fig. 2.5). Details on the simulation can be found in [17]. The simulation is being used to optimize the detector geometry, performance studies with truth data (e.g. background estimation), or for developing the event reconstruction.

In the simulation, muons are generated 3 m in front of the target with a beam profile as it is expected for the experiment. About 40 % of the generated muons are decaying on the target. The other muons decay in-flight before the target or miss the target. The output of the simulation includes various truth variables like kinematic or hit information. Furthermore, the expected response of the three sub-detectors is produced. The output data is organized in

frames of 50 ns length each. More details on the implementation of the tile detector in the simulation is given in section 3.6.

In the event reconstruction, the events are rebuilt based on the detector response. An important part is the track reconstruction, that deduces the particles trajectories from the hits in the pixel detector. The track reconstruction is implemented as a triplet based multiple scattering fit [27]. Triplets of hits are selected and MS is assumed to take place in the middle hit. The fit is done by minimizing MS. The equations for this can be linearized around the circle solution and thus a fast solving can be provided. In a next step, triplets are merged together to tracks. The vertex fit is currently a work in progress as well as the matching of a hit with the time information of the fibers. An algorithm for assigning the time-stamp from the tile detector to the corresponding track is presented and discussed in chapter 6.

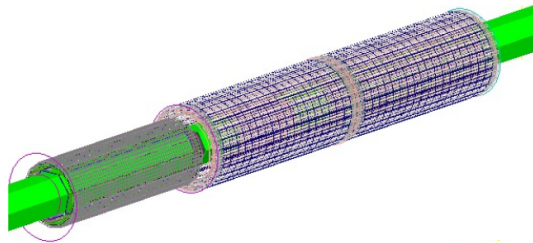
Figure 2.5.: The phase 1b detector as implemented in the simulation shown in a wire frame view. For the first station, the outer pixel layers (blue) are switched off, in order to see the tiles (gray). The beam line can be identified in green.

3. The Mu3e Tile Detector

Since the focus of this thesis is on the tile detector of the Mu3e-experiment, it will be described in more detail in this section. The purpose of this sub-detector is to provide a time-stamp with a resolution of $< 100\,\mathrm{ps}$ for the detected particles. This will be achieved by a combination of scintillating tiles and SiPMs.

In the following, basic information about scintillators and SiPMs as well as details on the design and read-out electronics of the tile detector are given.

3.1. Scintillators

Scintillators are materials that produce light when excited by ionizing radiation. There are different types of scintillators in all states of aggregation. In general, solid and liquid scintillators can be divided into organic and inorganic scintillators. Inorganic scintillators typically have a high light yield and are dense, leading to an excellent energy resolution while suffering from a long response time resulting in a poor time resolution. On the contrary, organic scintillators typically have a bad energy resolution while excellent time resolutions can be achieved. Since the major purpose of the tile detector is to deliver precise timing information, organic scintillators — in particular plastic scintillators — are the solution of choice and will be introduced in the following.

Plastic Scintillators

A plastic scintillator is a special kind of organic scintillator. It has a light yield of about 1 photon per $100\,\mathrm{eV}$ energy deposition, which is approximately proportional to the deposited energy for low enough energy densities. With a decay time of the order of ns and a much faster rise time, an excellent time resolution can be achieved.

Plastic scintillators consist of a mixture of various materials, which usually are: a base material, a primary flour, and a wavelength shifter. The working principle of a scintillator is shown in fig. 3.1. The base material is a plastic, for example polyvinyl toluene (PVT) or polystyrene

(PS). A particle depositing energy in the plastic is exciting electrons into higher molecular orbits. Disexcitation of those electrons emits photons in the UV regime of the spectrum. This process is called scintillation. Another important process happening in scintillators is fluorescence, which is the absorption of photons followed by an emission of light with a larger wavelength. In complex molecules the absorption and emission both take place over a broad range of wavelength. Thus, light that is emitted by the scintillator may undergo absorption shortly after. This effect is called *self-absorption*. Because of the quantum efficiency, this process shortens the attenuation length of the scintillator leading to a low light output. To avoid this, a *primary fluor* is added to the base plastic ($\approx 1\,\%$ by weight). The primary fluor has a gap between its absorption and emitting bands and thus is minimizing the self-absorption. Due to the strong coupling between the primary fluor and the base plastic, it also shortens the decay time and enhances total light yield. Nevertheless, a third component, a wavelength shifter (also *secondary fluor*), is needed to fully shift the light to the desired output wavelength and a reasonable attenuation length. Finally the light can be detected by a photodetector. [28] A study comparing different scintillators shows BC418 [29] to be best suited for the Mu3e tile detector [13].
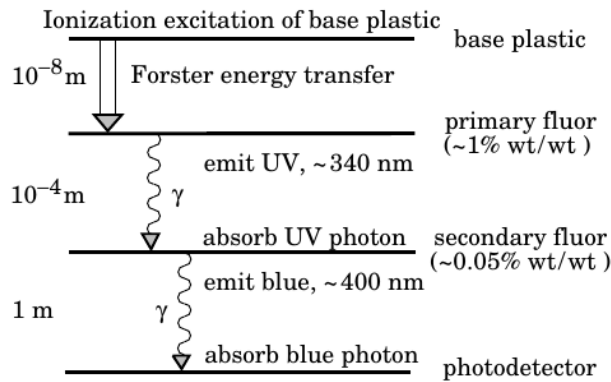

Figure 3.1.: Working principle of a plastic scintillator organized in four steps. The plastic serves as the base material producing UV photons by scintillation. The primary fluor enhances the attenuation length, reduces self-absorptions and the decay times. The secondary fluor finally emits photons with a wavelength optimized for detection in a photodetector. [28]

3.2. Silicon Photomultiplier (SiPM)

A SiPM [30] is a photon detector on a silicon basis. It has some advantages over conventional photomultiplier tubes (PMTs) namely the very compact design, the relatively low operating voltage usually being smaller than 100V, low costs, and its insensitivity to magnetic fields [31]. These features make SiPMs highly suitable for particle physics experiments like the Mu3e experiment.

SiPMs consist of an array of typically 100 to 1000 avalanche photodiodes (APDs) connected in parallel. The APDs are operated at a high reverse bias voltage only a few volt below breakdown voltage (*geiger mode*). One possible doping structure is shown in fig. 3.2. Photons reaching the sensor produce electron hole pairs via the photoelectric effect, which then are drifting in the electric field of the diode due to its doping structure. At the multiplication region, the electric field is so strong that secondary electron hole pairs are created by impact ionization. Those secondary electrons and holes again undergo high acceleration and can generate further electron hole pairs leading to a self-sustaining *avalanche*. A high-ohmic resistor quenches the avalanche by a voltage drop.

A picture of a SiPM is shown in fig. 3.3a. The amplitude of the output signal of the SiPM is the sum of the signals of the APDs (also called *pixel*). This means that below saturation, where all pixel are firing, the amplitude of the signal scales in first order with the amount of detected light as can be seen in fig. 3.3b.

There are models from different manufactures, with varying pixel sizes, active areas, and other properties. The Hamamatsu MPPC S12572-050C [32] with an active area of $3\,\mathrm{mm} \times 3\,\mathrm{mm}$ and 3600 pixels is best suited for the requirements of the Mu3e tile detector [13].
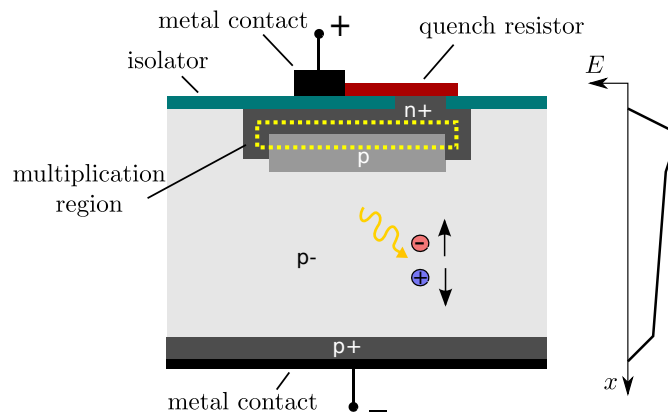

Figure 3.2.: Schematic view of an APD with an $n^+\, p\, p^-\, p^+$ doping structure. The resulting electrical field E inside the diode is shown on the right. Photons hitting the detector can produce electron hole pairs due to the photoelectric effect. The electron drifts upwards in the electric field. Due to the high electric field in the multiplication region, an avalanche is triggered by impact ionization. The quenching of this self-sustained process is realized by a voltage drop over a resistor. (Adapted from [33])
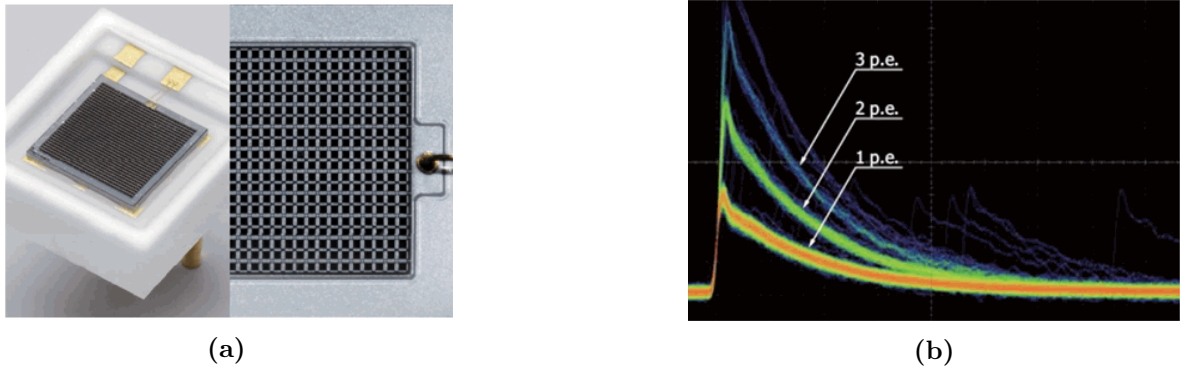
<div align="center">(a)   (b)</div>

Figure 3.3.: **(a)** Picture and close-up of a SiPM. In the close-up, the different pixels can be clearly identified. **(b)** Overlay of several SiPM signals. The number of pixels that detected a photon determines the amplitude of the signal. The one- and two-photon signals can be clearly separated. (Both taken from [34])

3.3. Design of the Mu3e Tile Detector

The current design of a station of the tile detector is a 14-fold symmetry shown in fig. 3.4. On each edge there are four scintillating tiles in phi-direction, leading to 56 tiles on each ring. There are 60 such rings in z-direction which make a total of 3360 tiles per station. Underneath each tile, there is a SiPM located for detecting the light the particles produce in the scintillating tiles. A submodule is formed by 32 tiles (see fig. 3.5a). The read-out electronics are directly attached to the SiPMs with a 7-fold symmetry. They are hold by an aluminum support structure. Each read-out module reads out 32 SiPMs (i.e., one submodule). The dimensions of the tiles are shown in fig. 3.5b. They have a height of 5 mm, expand 6 mm in z-direction, and have a width of about 6.7 mm. Tiles at the edges are slightly wider at the top (about 7.8 mm). While smaller tiles would reduce the pile-up, they would also increase the number of channels and reduce the light output leading to smaller output signals. Each station has a length of 36 cm with a gap of 4 cm between them. More details on the design of the tile detector can be found in [13].
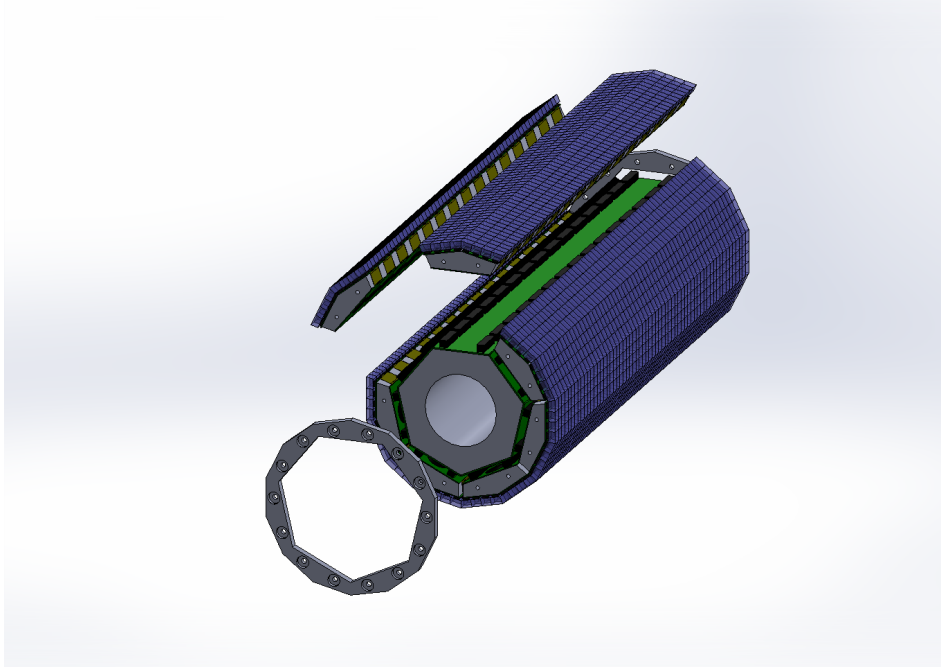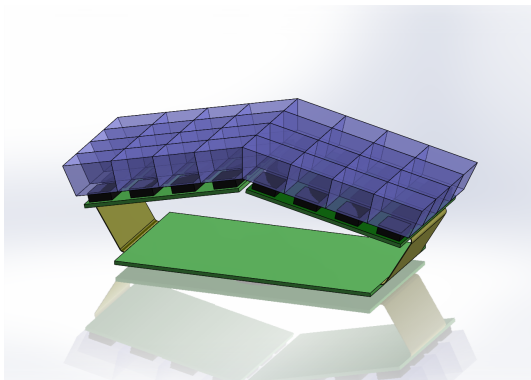
Figure 3.4.: Design of a station with the Mu3e tile detector. The beam-pipe (gray) has a 7-fold geometry which supports the read-out electronics (green). On top of the read-out electronics the SiPMs are placed with the scintillating tiles (blue) in a 14-fold symmetry. The station consists of 3360 tiles in total. [13]

(a)
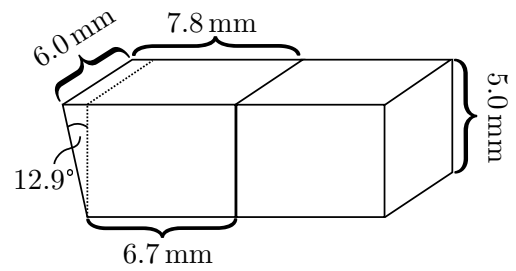
(b)

Figure 3.5.: **(a)**: Submodule of the Mu3e tile detector. Each submodule consists of 32 tiles and is read out by the electronics underneath. [13] **(b)**: Dimensions of the scintillating tiles. To avoid gaps at the edges of the detector, the tiles at the edges are slightly larger on the top than the other tiles.

3.4. Read-out Electronics — STiC

The SiPMs are read out with STiC (Silicon Photomultiplier Timing Chip) [35]. STiC is a mixed-mode application specific integrated circuit (ASIC) particularly designed for precise timing. The basic working principle is shown in fig. 3.6. STiC has two thresholds, one at a low level for precise time measurements and a second one typically at a higher level for measuring the charge of the signal by a time over threshold (TOT) measurement. These thresholds discriminate the signal into two trigger pulses, which are joint by a logical exclusive OR (XOR) to a single signal. In the combined signal the time information is preserved as the rising edge of the time trigger, while the energy information is encoded as the time between the falling edge of the time trigger and the rising edge of the energy trigger. A time to digital converter (TDC) digitizes the combined signal with a bin size of 50.2 ps. The TDC is realized by a coarse counter (CC) with a bin size of 1.607 ns and a fine counter subdividing the coarse counter period in 32 bins. Upon hits, the time stamps of the individual TDC channels are stored in a first-in-, first-out-memory (FIFO). The events are transmitted in frames to the data acquisition (DAQ) every 6.4 μs.

The second version of the chip (STiCv2) is fully characterized [36]. The time jitter of the chip was shown to be 45 ps. A new version of the chip (STiCv3) has various improvements, e.g., an improved time jitter of 37 ps [37]. Furthermore a tail-cancellation is implemented that is expected to reduce the dead time of events and thus reducing pile-up. For the Mu3e experiment a special version will be designed to fit the given requirements.

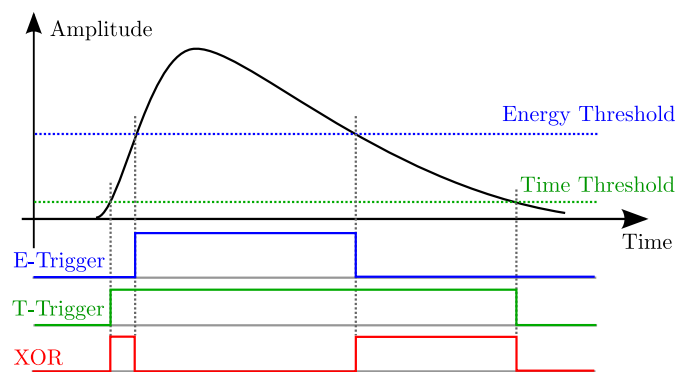**Figure 3.6.:** Simplified working principle of STiC. The SiPM-signal is discriminated by two thresholds, the energy- and the time-trigger. Both trigger signals are combined by an XOR logic leading to two trigger pulses of a combined signal. The time information is preserved in the first rising edge, while the energy information is stored in the time difference of the inner edges between both pulses. (Adapted from [37])

3.5. Time Resolution

As stated above, the required time resolution of less than $100\,\mathrm{ps}$ is the key feature of the tile detector. The time resolution is defined as the width of the distribution of detection times relative to a trigger signal. Besides the excellent read-out electronics, an optimized analysis is also required to reach this goal. An effect that has to be taken into account is the dependence of the time-stamps on the height of the signals, the *time-walk effect*, shown in fig. 3.7. Under the assumption of a constant rise time, the rising slope of the signal gets steeper for a higher amplitude and thus the signal crosses the timing-threshold faster, leading to an earlier time-stamp. This effect adds up to the time-resolution, but can be partially countered by an offline correction with respect to the amplitude of the signal.

Besides the intrinsic time resolution of a SiPM, which is discussed in [38], electronic noise σ_{el} on the signal has a major influence on the total time resolution of the system. The uncertainty σ_t^{el} from electronic noise on the time-stamps is approximately inverse proportional to the slope S of the signal [39]:

$$\sigma_t^{(\mathrm{el})} = \frac{\sigma_{\mathrm{el}}}{S}. \tag{3.1}$$

This means in particular that a higher signal has a better time resolution than a lower one. A geometrical intuition of this effect is illustrated in fig. 3.8.

However, it was shown experimentally that the overall time resolution σ_t as a function of the number of fired pixel N is better described by the poissonian law until the electronic noise dominates [13, 30]:

$$\sigma_t \propto \frac{1}{\sqrt{N}}. \tag{3.2}$$

In order to compare the time-stamps from different SiPMs in the detector, they have to be calibrated relative to each other. An uncertainty in the calibration would also add up to the overall time resolution of the detector. The calibration of the tile detector will be discussed in detail in chapter 7.

At a testbeam campaign [13], the total time resolution of a tile-SiPM-STiC-system was measured to be $60\,\mathrm{ps}$. This is already better than the original requirement for the tile detector.
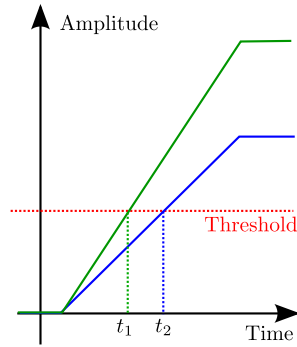
Figure 3.7.: Time-walk effect: The time the signal crosses a constant threshold depends on the hight of the signal. The signal with the higher amplitude shown in green produces the earlier time-stamp t_1. (Adapted from [38])

Figure 3.8.: Electronic noise on the signal has a contribution $\sigma_t^{(\mathrm{el})}$ to the time-resolution of the detector. For a higher, and thus steeper, signal the influence of the electronic noise is suppressed. (Adapted from [39])

3.6. The Tile Detector in the Geant4 Simulation

The Mu3e tile detector is fully implemented in Geant4 and part of the full detector simulation. The tiles are implemented as a plastic material. The light propagation 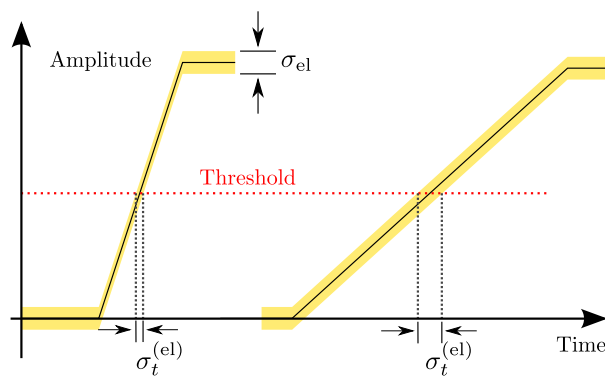in the scintillator and the SiPM response are measured and simulated separately, and fed into the simulation in a parametrized form [13].

The deposited energy is calculated and a truth time-stamp is generated for every particle hit. If a second hit is generated within the dead time of a tile, the energies of both hits are added, but no new time information is created. Furthermore, both, the energy and the time-stamp are digitized. This means, that the energy information is smeared out by the expected energy resolution of the tile-SiPM-STiC-system. Hits with an energy lower than the energy threshold (about 10 % of the average energy deposition) are not considered anymore. Additionally, an uncertainty is added to the truth time-stamp due to limitations in the time resolution. The time-resolution is implemented as a fixed jitter produced in STiC and a contribution from the SiPM, which is proportional to one over the square root of the signal height.

Part II.

Calibration Studies for the Mu3e Tile Detector

4. Data sets and simulation procedure

The data sets used in the following were generated with the Mu3e full detector simulation [1]. Unless written otherwise, the standard configuration and digitization parameters were used. All data was sorted by the Mu3e-Sorter. Because the digitized hits in the detector systems are written out at the time when the corresponding detector signal ends, this information can thus be in a different order then the actual hit occurance. For the tile detector with a TOT of over 200 ns, subsequent hits may be distributed over many frames. The Mu3e-Sorter solves this problem by sorting the information into the frames where the signal started. Next, the data is processed by the Mu3e-track-reconstruction.

Throughout this thesis, there are two main data sets under investigation — one for phase 1b and the other for a phase 2 configuration. The phase 1 data set contains 100,000 frames ($= 5\,$ms) at a rate of $2.5 \times 10^8\,\mu/\text{s}$. This corresponds to 1,250,000 generated muons of which 496,000 decayed on the target. For the phase 2 setting configuration, 5,000 frames ($= 25\,\mu\text{s}$) were simulated, leading to 1,256,000 generated muons of which 500,000 decayed on the target.

---

[1] version 2.2.0, committed at 18.12.2014

5. Preliminary Studies

This section presents studies that were performed to gain a better understanding of the simulation, reconstruction and analysis. The measurement of the dead time of a tile-SiPM-STiC system is an important parameter that has to be supplied to the simulation. Furthermore, the rate that is expected in the tiles and the corresponding pile-up is studied, as well as the topology and reconstruction of clusters of hits in the tile detector. The kinematics of particles hitting the tile detector are discussed at the end of this chapter.

5.1. Dead Time Measurement

The dead time is an important property for detectors measuring at high particle rates. It is the time the system needs after detecting a hit to recover and to be able to detect another hit. If the dead time is too long, events might be lost. Effects like this are called *pile-up* and will be also discussed in section 5.2.

The setup for the dead time measurement is shown in fig. 5.1. A sodium source is placed in front of a plastic scintillator (NE110) with a SiPM ($3\,\text{mm} \times 3\,\text{mm}$, $50\,\mu\text{m}$ pitch) attached. The system is read out with the STiCv2 chip, which is powered with a $12\,\text{V}$ operating voltage. The SiPM is operated at a $73.5\,\text{V}$ high voltage (HV). STiCv2 is mounted on a special mainboard that is handling the power supplies. Furthermore, the mainboard contains a field-programmable gate array (FPGA) which transmits the data to a PC that runs the DAQ software.

The time period between two events (i.e., the time difference between two subsequent hits) is calculated and ordered with regard to the energy of the first hit. Figure 5.2a shows the periods for events where the first hit has an energy between 50 and 55 coarse counter (CC) values. The distribution is exponentially falling, as expected for a poissonian process. The beginning of the distribution defines the dead time for this energy range. This is done over the whole energy range and the dead time over the energy of the first pulse is shown in fig. 5.2b. The dead time is linear with respect to the energy of the first pulse with a slope of $1.642\,\text{ns} \pm 0.026\,\text{ns}$, which is in a two sigma range of the conversion factor between CC and ns of $1.607\,\text{ns/CC}$. This proves the linearity of STiCs dead time with the TOT of the signal. The intersection of the linear fit with the y-axis is at $42\,\text{ns} \pm 2\,\text{ns}$ and equals the dead time of the TDC.

Unfortunately, due to the poor energy resolution of the plastic scintillator it is not possible to give an exact conversion factor between coarse counter values and energies in keV. Nevertheless, a rough estimate can be gained. For STiC the CC is linear with the charge of the signal for values larger than 20 CC with a slope of $\approx 1.4\,\text{CC/pC}$ [35]. The charge Q of a pixel of a SiPM is given as the product of the over voltage $(U_{\text{bias}} - U_{\text{break}})$ and the capacity of a pixel C_{pixel} [40]:

$$Q_{\text{pixel}} = C_{\text{pixel}} * (U_{\text{bias}} - U_{\text{break}}) \tag{5.1}$$

In this measurement, an over voltage of 2.5 V and a pixel capacity of about 100 fF [40] lead to $Q_{\text{pixel}} = 250\,\text{fC}$. Thus, the conversion factor between CC and fired pixels can be estimated for the used settings to $1\,\text{CC} \approx 3.6$ fired pixel.

The SiPM-signals in the experiment are expected to consist of a few hundred fired pixels. In a test-beam campaign, signals with an energy of slightly over 100 CC were measured [13]. This corresponds to a dead time of about 200 ps, which is used as a parameter for the dead time of the average hit in the simulation of the tile detector.
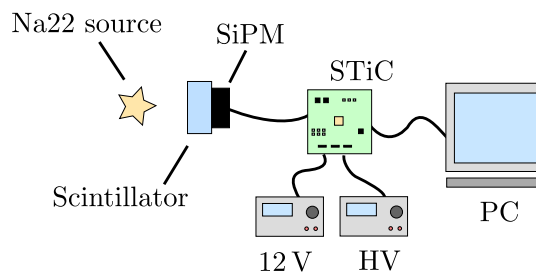

Figure 5.1.: Setup of the dead time measurement. A sodium source is put in front of a scintillator. The scintillation light is detected by a SiPM which is read out by STiCv2.

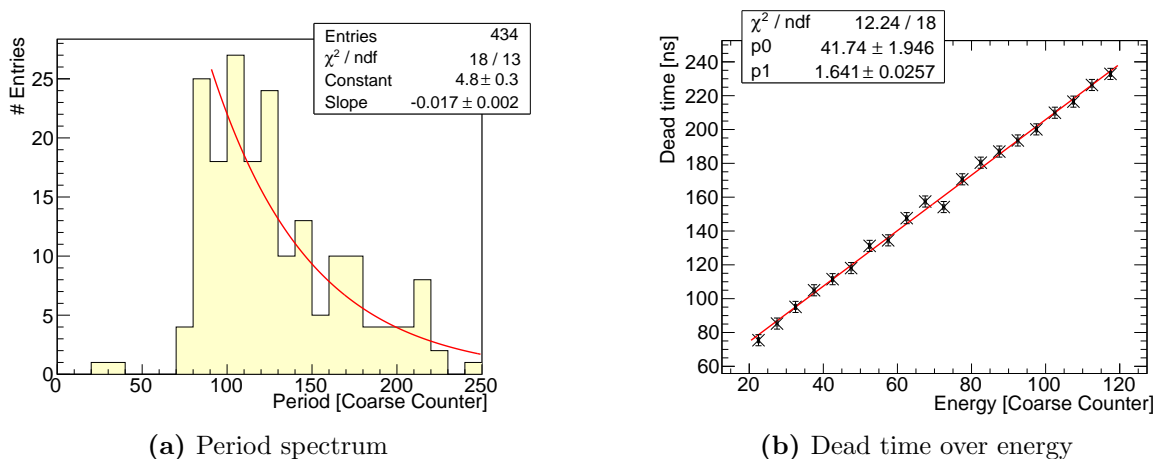(a) Period spectrum

(b) Dead time over energy

Figure 5.2.: (a) Time differences between two subsequent pulses. The energy of the first hit is required to be between 50 CC and 55 CC. (b) Dead time over energy. The slope of 1.64 ns is consistent with the conversion factor between CC and ns. The intersection with the y-axis at 42 ns is the dead time of the TDC.

5.2. Pile-up

Effects of simultaneous events in a detector influencing each other are called pile-up effects. In the following the term pile-up will be used to describe the fact, that the tile detector cannot detect two consecutive hits due to the dead time. In such a case, the information of the second hit is lost. The fraction of pile-up events N_{pileup} relative to the number of total events N_{total} can be calculated by the rate in the tiles and the dead time:

$$F_{\text{pile-up}} \equiv \frac{N_{\text{pile-up}}}{N_{\text{total}}} = 1 - \frac{1}{\exp(\text{rate} * \text{dead time})} \tag{5.2}$$

Figure 5.3 shows the rate and pile-up in the simulation for the tiles over their z-position (i.e. the distance of the target along the beam line) for phase 1 and phase 2. The asymmetry in rates of the up- and downstream side of the target arises from the polarization of the muons; as shown in section 1.2, the decay of polarized muons has a preferred direction. Tiles near the target generally have a higher rate of hits than those far away. This is due to the low energy of the electrons and thus their rather small bending radii. The rising tail for the phase 2 data set on the beginning of station 1 is due to in-flight decaying muons. These effects are discussed in more detail in [13].
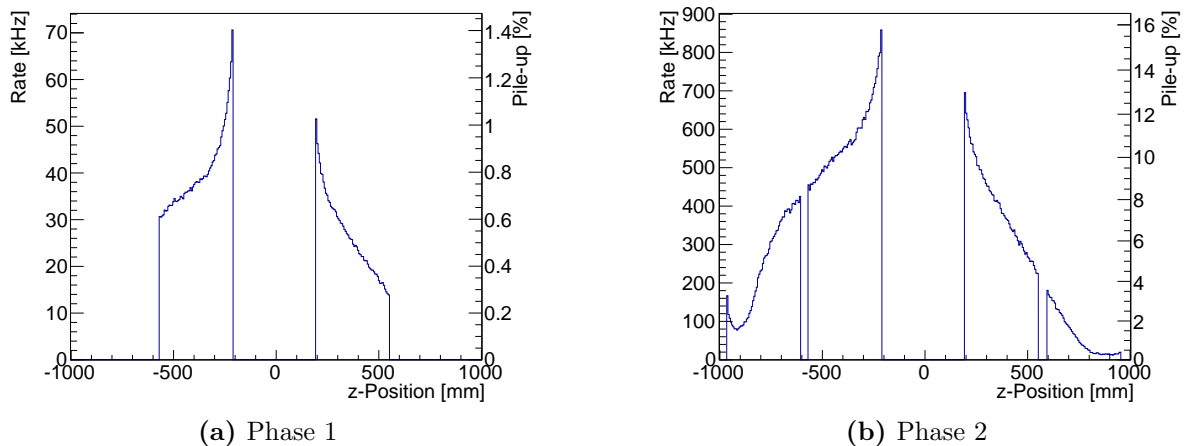

(a) Phase 1   **(b)** Phase 2

Figure 5.3.: Rate and pile-up in the tiles over their z-position for phase 1 **(a)** and phase 2 **(b)**. Shown is the mean value for all 56 tiles with the same z-position on one ring. The target is located at z-position 0. The gap between station 1/2 and 3/4 for phase 2 can be identified at a z-position of ± 600 mm.

The mean pile-up for phase 1 is $0.60\,\%$ and $8.8\,\%$ for phase 2. While in phase 1 pile-up plays a minor role, many tiles have more than $10\,\%$ pile-up events in phase 2. Thus, pile-up has a major influence on the detector performance and needs to be considered in the following analysis for phase 2.

5.3. Cluster

If several detected signals in neighboring scintillating tiles are produced either directly or indirectly by the same particle, they are called a *cluster*. The direct process would be a particle coming in under a flat angle in either φ- or z-direction and thus flying through more than one tile. An indirect hit could be for example produced by a secondary electron generated in the tiles. Figure 5.4 shows the number of hits in different tiles generated by a single particle. Over 60 % of the particles are generating more than one hit in the tiles, so those events are a significant contribution to the rate. In the following, the distributions of hits in a cluster in space and time are given. They are necessary for the reconstruction of clusters in the tile detector.
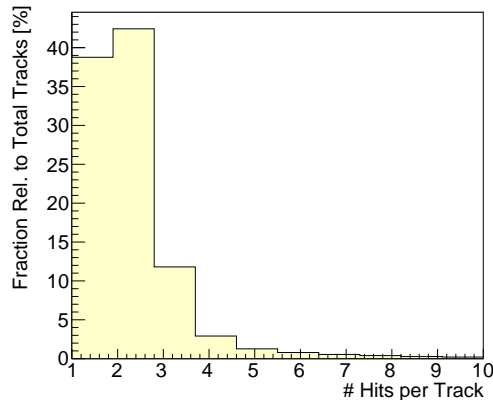

Figure 5.4.: Number of hits in different tiles generated by one primary particle from the target (i.e. the cluster size) for the phase 1 setting. Over 60 % of the particles are generating more than one hit in the tiles with most generating two hits.

The distribution of time differences before digitization (i.e., the truth time) between two consecutive hits in a cluster is shown in fig. 5.5a. In most cases, the time difference between two sequential hits is smaller than 50 ps. The distribution is quickly decreasing after 25 ps. The narrow peak at 20 ps is generated by particles that are completely traversing at least one tile. The length of the tiles in z-direction is 6 mm. Thus, a particle needs at least $6\,\mathrm{mm}/c = 20\,\mathrm{ps}$ to pass through. Most entries for time differences larger than 50 ps are derived from particles leaving a tile at the inner side and recurling back into another tile after a few cm. After the digitization process, the distribution is smeared out by the time resolution of the detector, resulting in an exponentially falling distribution (see fig. 5.5b).

The maps in fig. 5.6 show the spatial distribution of cluster hits relative to the first impact of the particle in the tiles for the second and third station in the phase 1 setting. Each rectangle represents a tile and the first hit is always in the red rectangle. The number in each tile represents the probability of a hit at the corresponding position. For both stations, the next tile in z-direction also generates a signal with a probability of 45 %. For φ-direction this value is lower (12 % to 14 %), due to the steeper incident angle in this direction.

(a) Before digitization
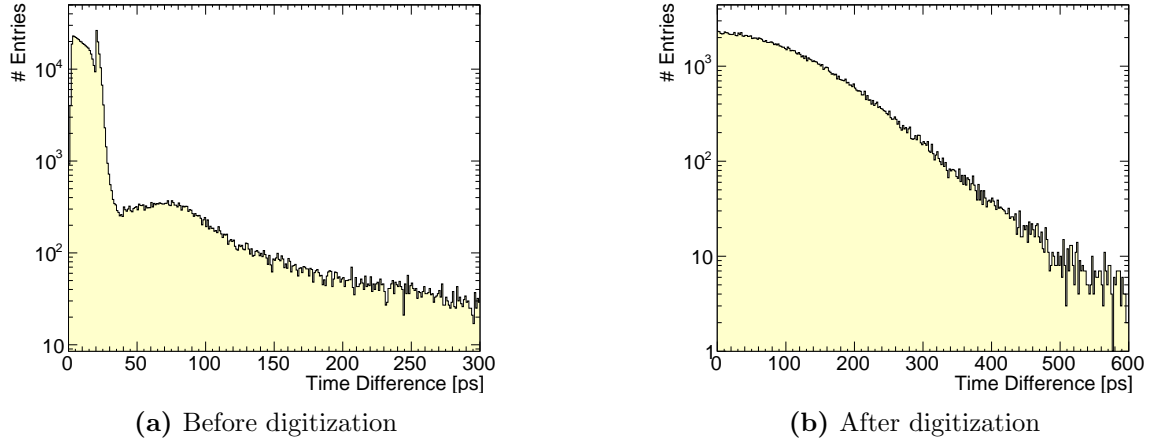
(b) After digitization

Figure 5.5.: Time differences of consecutive hits in one cluster before digitization **(a)** and after digitization **(b)**. Because of the time resolution of the detector, the true time differences are smeared out resulting in an exponentially falling distribution. Note the different ranges on the x-axis.

(a) Station 2
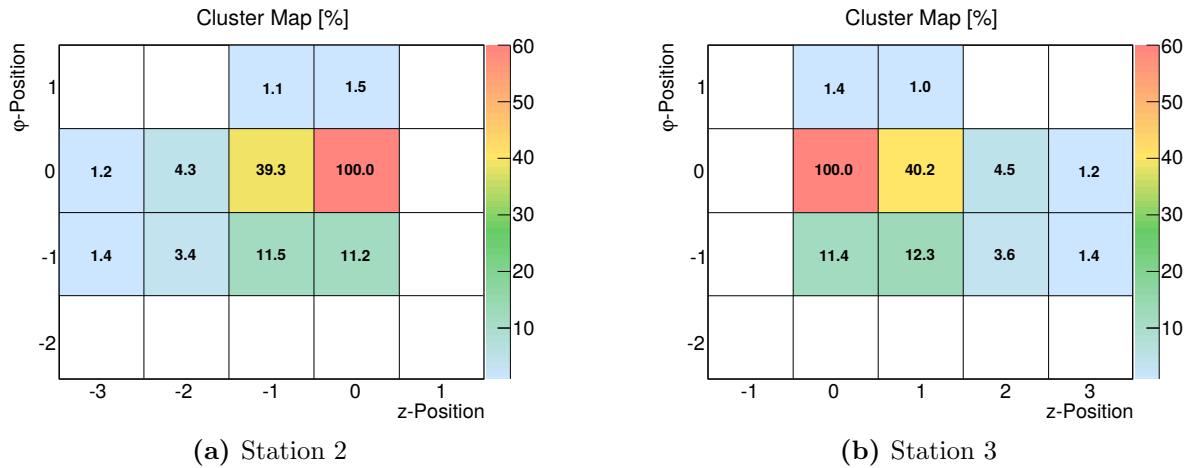
(b) Station 3

Figure 5.6.: Cluster maps for station 2 **(a)** and station 3 **(b)** in a phase 1 setting. The detector is shown as a flat projection. The first hit of a cluster is filled to the position (0,0) on the map. The other bins are filled with the corresponding fraction of hits relative to the first hit. For simplicity entries with a fraction of less than one percent are not shown. The phase 2 data set shows similar results that can be found in appendix A.

Cluster Reconstruction

An excellent assignment of secondary hits to the primary hit can eventually help dealing with pile-up, especially for the high rate in phase 2. Without using the truth information, one has to think about how to exactly find and define a cluster. This procedure will be discussed in the following. As with most analysis, this is a trade-off of *efficiency* (that is the fraction of hits correctly added to a cluster) and *fake rate* (meaning the inclusion of false hits into a cluster, i.e., false positive).
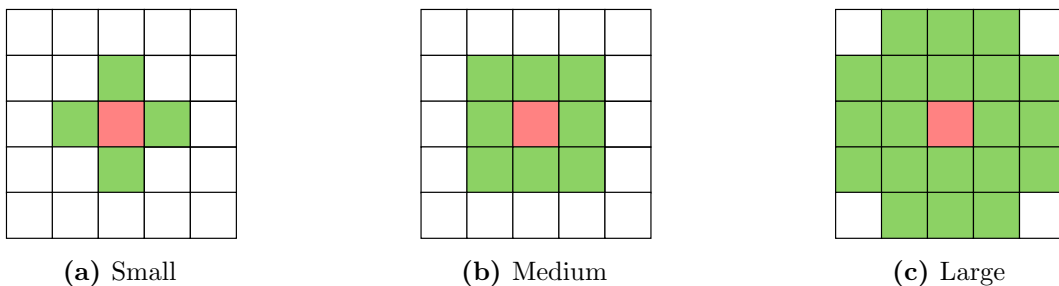

(a) Small   **(b)** Medium   **(c)** Large

Figure 5.7.: Definition of neighboring tiles for a small, medium and large mask in a flat detector projection. The red tile in the center marks the reference tile. For each mask, all green tiles are defined to be neighbors.

Because of the narrow time distribution of the hits in one cluster, those hits are required to be in the same frame for the reconstruction. Increasing the search window to two or even more frames will not significantly increase the efficiency, but rather increase the fake rate. All hits in a frame are compared to each other and are added as a cluster if they are *neighbors* in a spatial sense and if they are close in time. If one hit is already in a cluster and a second one meets the mentioned requirements it will be added to this cluster.

First of all, it has to be defined what is meant by a neighbor. In this section three different masks are compared, a small one, a medium, and a larger one as shown in fig. 5.7. The small mask only considers the direct neighbors in φ- and z-direction, while the medium mask includes all eight direct neighbors of a tile, and the large mask covers a large area. A large area has the advantage of finding constituents of a cluster, even when they are split up by not detected hits, for example due to pile-up or a too low energy deposition.

Figure 5.8 shows the fraction of hits in a cluster that are produced by different primary particles, meaning they do not belong to the cluster and were reconstructed incorrectly (called fake rate, red), as well as the fraction of hits that are missed in the cluster reconstruction (i.e., $1 -$ efficiency; blue). In this case, the efficiency is defined as the number of hits that are correctly clustered to the primary hit, compared to truth data. In this plot, hits further than four tiles away from the primary hit are ignored, because it is more important to correctly cluster the near neighborhood of the first impact with the tiles as this contains the main timing and energy information. Both measures are plotted over the time window in which two hits in a cluster are required to be for all three types of masks.
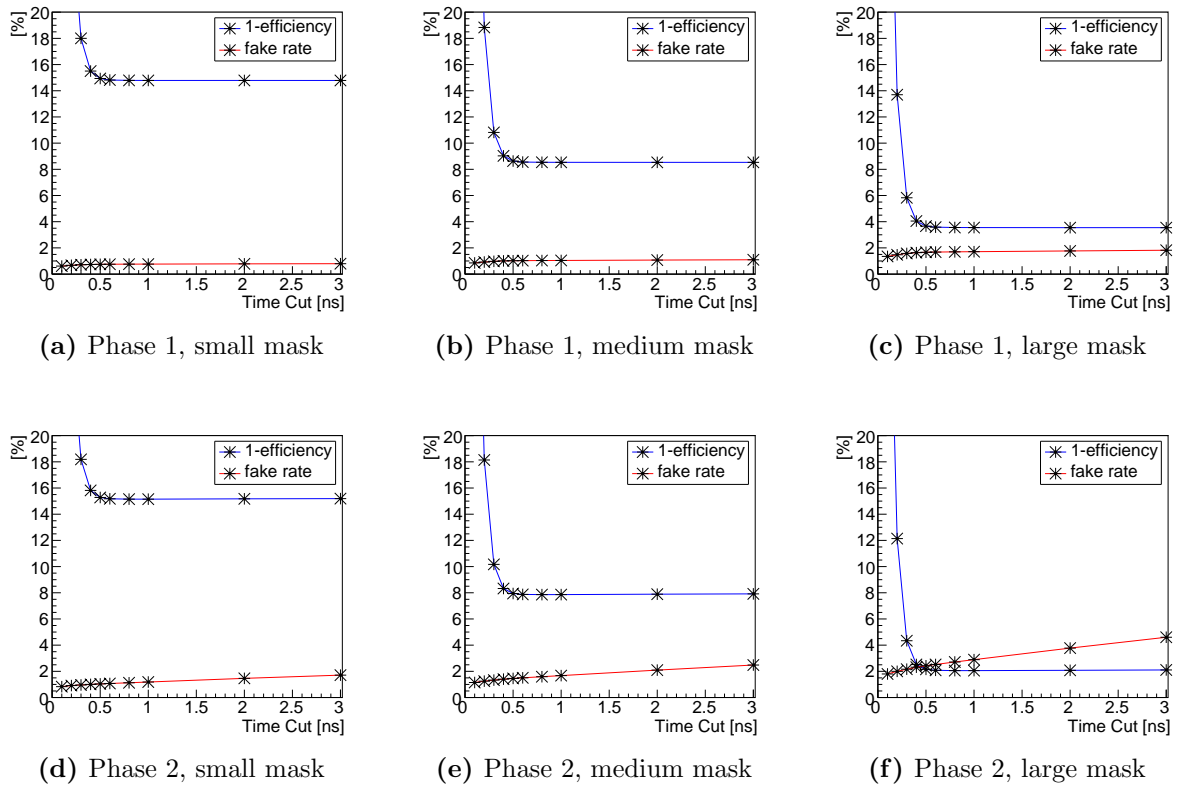
(a) Phase 1, small mask

(b) Phase 1, medium mask

(c) Phase 1, large mask

(d) Phase 2, small mask

(e) Phase 2, medium mask

(f) Phase 2, large mask

Figure 5.8.: Comparison of three different neighbor-masks for the efficiency and fake rate of the cluster reconstruction over the time cut of two particles in a cluster (phase 1 and 2). A larger mask significantly increases the efficiency of the reconstruction but also slightly increases the fake rate. For phase 2 the increase in fake rate is much more prominent.

It can be seen that the fake rate increases moderately with the size of the time window, nevertheless being quite small ($\approx 1\%$). The fake rate also slightly increases with the size of the mask. This effect is much more pronounced in the phase 2 data set, due to the larger hit density. For a larger time window, the probability of clustering hits that do not belong to the cluster is increased. The fraction of not clustered hits shows the opposite behavior. It quickly decreases with the time window reaching saturation at 0.7 ns. The effect of the size of the mask is much more dominant. It decreases from 15 % for the small mask to 4 % for the large mask. Comparing the results for the phase 2 setting with the phase 1 setting, the efficiency does not change dramatically.

A time coincidence window for the hits in a cluster between 0.5 ns and 1 ns is considered optimal. However, the choice of the right mask for neighbors is a trade-off between fake rate and efficiency, and depends on the needs of the analysis.

5.4. Kinematics

This section aims at analyzing the momentum distribution of particles hitting the tile detector. The radius of a particle r in a magnetic field ($B = 1\,\mathrm{T}$ for Mu3e) can be calculated relative to the transverse momentum p_T by the following equation:

$$\frac{r}{\mathrm{meter}} = 3.3 \times \frac{\left(\frac{p_T}{\mathrm{GeV}}\right)}{\left(\frac{|q|}{e}\right)\left(\frac{B}{\mathrm{Tesla}}\right)}, \tag{5.3}$$

with $\frac{|q|}{e} = 1$ for electrons and positrons. The most outer pixel layer has a transverse distance from the center of the detector of $8.2\,\mathrm{cm}$. This means that the radius of a particles trajectory has to be at least $4.1\,\mathrm{cm}$ on average in order for to particle to be in the acceptance of the outer pixel layer. Using eq. (5.3), this results in the following constraint on the transverse momentum of the electron:

$$p_T \equiv \sqrt{p_x^2 + p_y^2} > 13\,\mathrm{MeV}. \tag{5.4}$$

Figure 5.9 illustrates the acceptance of the detector for tracks with different transverse momentum. The kinematics for the phase 1 data set (i.e., mainly Michel decays) are presented in fig. 5.10. Shown are the momentum distributions for reconstructed tracks that hit the tile detector. The starting point of the distribution of the transverse momentum (fig. 5.10a) is in agreement with the results obtained analytically above. The sharp edge at the upper limit of the distribution is defined by the Michel spectrum. Besides the constraint on the transverse momentum, the particle is required to have a certain momentum in z-direction. Figure 5.10b shows that most particles have at least $10\,\mathrm{MeV}$ and are thus able to reach the tile detector. The total momentum of the particles (fig. 5.10c) is for most particles at least $20\,\mathrm{MeV}$. The upper limit is again given by the edge of the Michel spectrum. The decrease in the distribution for a momentum of $p > 40\,\mathrm{MeV}$ is due to the end of the station for the phase 1 setting and not observed in the phase 2 data due to the additional stations (see appendix C for the corresponding figures for phase 2).
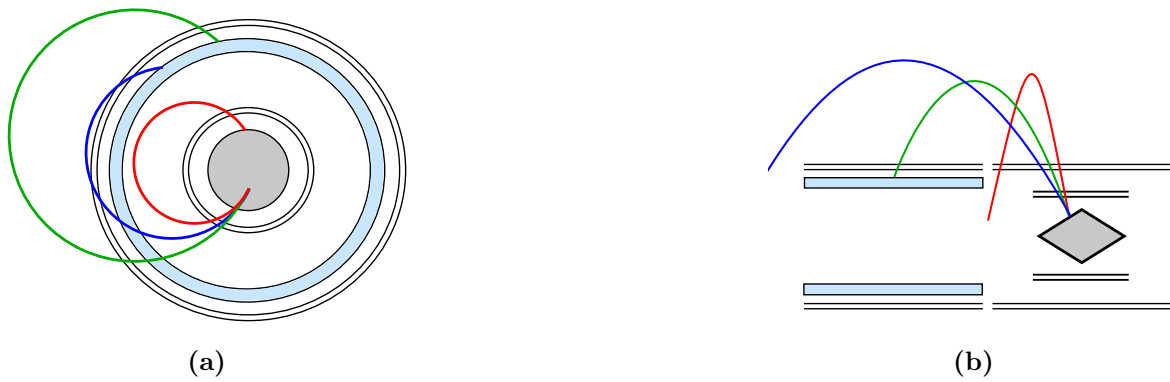
(a)   (b)

Figure 5.9.: Cross section through the detector. **(a)** Three tracks are shown with different transverse momenta p_T. The red track has a low transverse momentum and is missing the tile detector (light blue). The blue and green tracks have a high enough transverse momentum to be in the acceptance of the outer pixel layer (black circles) and the tile detector.
(b) Three tracks with different p_z. Just the green track is reaching the tile detector, the other two have a too low (red), or a too high (blue) p_z. Note that these sketches are not to scale.

(a) Transverse Momentum p_T

(b) Momentum in z-direction p_z
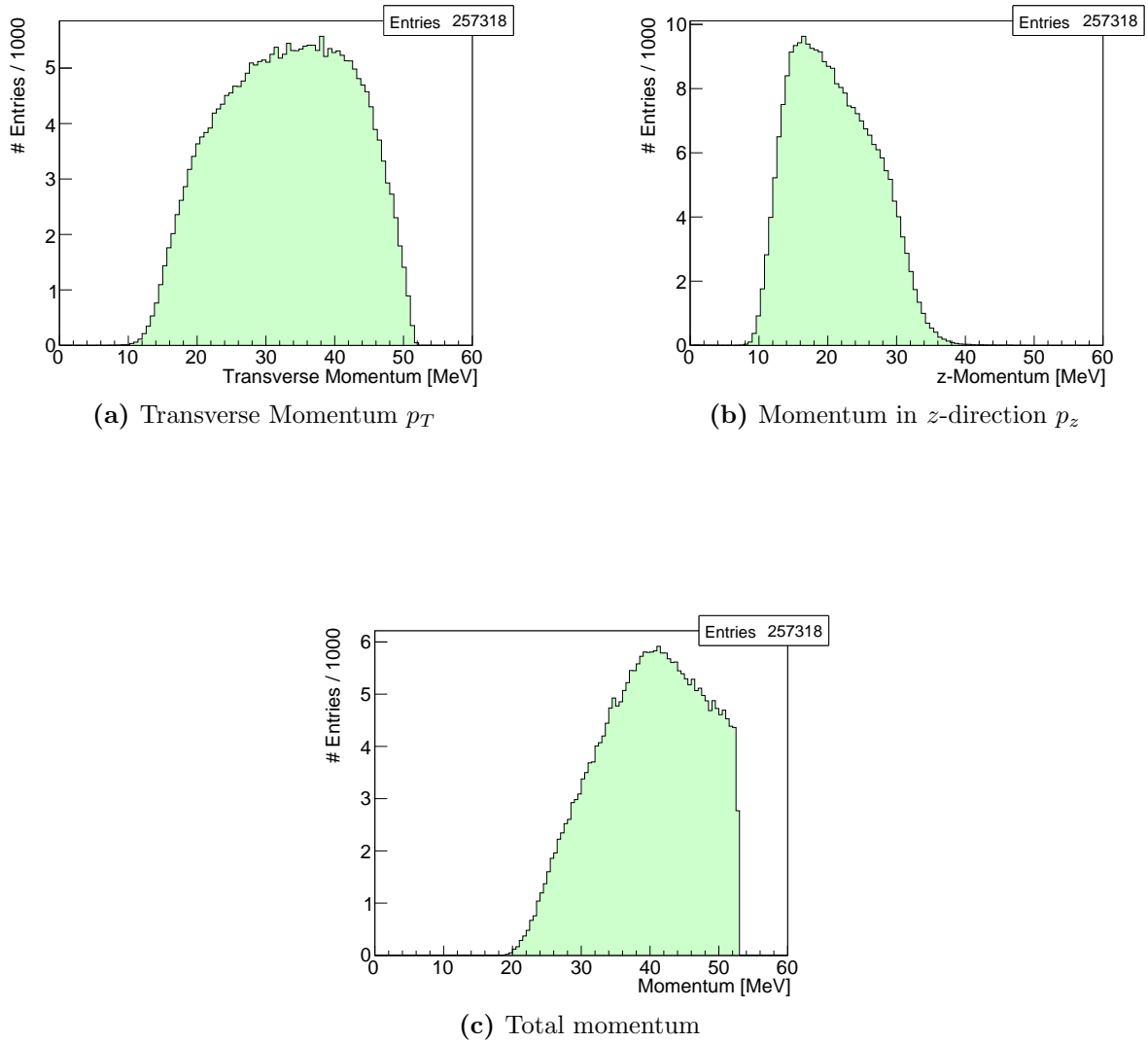

(c) Total momentum

Figure 5.10.: Momentum distribution for reconstructed tracks that hit the tile detector. Shown is **(a)** the transverse momentum, **(b)** the momentum in z-direction, and **(c)** the total momentum.

6. Track-Tile Matching

An essential step towards a full event reconstruction is the track-tile matching, meaning the assignment of time-stamps from the tile detector to the corresponding tracks. This is being done by estimating the impact position of the track on the tiles and selecting a corresponding time-stamp from the tiles in the region around this position. The challenges for the algorithm are lying in the high efficiency that is required, especially at high rates of over one billion decaying muons per second. In the following, this procedure will be described in detail and the performance will be discussed.

6.1. Data Selection

The starting point of the track-tile matching is the track reconstruction. Correctly reconstructed tracks are selected requiring hits in exactly six different pixel layers and, in addition, the last hit in the pixel layer has to be in a recurl station. This ensures the tracks to be able to hit the tile detector. After this selection there are 42% (257,000 / 612,000) tracks left for phase 1, and 35% (62,000 / 179,000) for phase 2. The much lower number of reconstructed tracks for the phase 2 data set is due to the increased rate.

6.2. Estimation of the Impact Position

The tracks of the particles are in first order describing a helix. The state of a particle path is thus fully defined by the two angles θ and ϕ (fig. 6.1), the position in the last pixel layer hit and the 3D-radius of the reconstructed helix. All the information is provided by the track reconstruction. The helix is then propagated using the watson-package [41].
The detector symmetry defines 14 planes. To get a prediction of the impact position of a particle on the tiles, the intersection point of the helix and the two nearest tile planes is calculated as shown in fig. 6.2. In most cases, exactly one of the two intersection points is

located outside of the detector (gray star in the figure) and the other one is within the borders of the detector (large, yellow star in the figure). The latter one is used as the predicted impact position of the track. However, there are also tracks that have no intersection within the detector borders with both planes. Figure 6.3 shows that the z-position of those hits in the last pixel layer is always at the end of the station. Those tracks have no impact with the tiles because of their momentum in z-direction; they are hitting the pixel layer but overshoot the tiles. These are 1.2 % of tracks for both data sets.

The geometrical distance between the predicted impact position and the true impact is shown in fig. 6.4. The contributions to this difference are mainly due to the uncertainty of the track reconstruction and possible multiple scattering (MS) occurring in the last pixel layer. The distribution has its maximum at less than 100 μm. Only very few tracks have the true impact position further away from the predicted position then 1 mm. This is ^{1}/$_6$ of the tile length and sufficient for the assignment of a time-stamp.

6.3. Assignment of a Time-Stamp

The tile which is closest to the estimated impact position is defined as the tile of first impact. However, the estimated tile of first impact does not necessarily provide the best time-stamp for the track. There are various error sources influencing the result. Because of direct pile-up or a too low energy deposition, the actual hit might not be detected in the estimated tile. Also an inaccurate estimate of the impact position might result in an incorrect assignment of a time-stamp to the track. Figure 6.5 shows the position of the true tile of first impact relative to the estimated one. For over 88 % of the cases both coincide. The remaining 12 % are distributed around the predicted tile. As expected, the results for station 2 and 3 are mirrored by the φ-axis. The results for stations 1 and 4 for the phase 2 data set look similar and can be found in appendix B.

The correct time-stamp for each track is determined by searching in a mask which assigns priorities to the tiles around the predicted tile. A mask that is too large may include more false positives, especially for phase 2, while a too small mask may miss hits. The mask that shows the best results for the simulation data is shown in fig. 6.6. This mask leads to ambiguities, where more than one track have a hit in the mask region in the same frame. While this is a sub-percent problem for phase 1, there are hits from more than one track with a probability of about 10 % for phase 2. To solve these ambiguities and to have the best chance of picking the right hits, the tiles in the mask region are checked for hits in a certain order indicated by the numbers in fig. 6.6. These numbers are deduced from the probabilities in fig. 6.5. If there is a hit in the predicted tile of first impact (red tile in fig. 6.6), the time information of this hit is assigned to the track. Else, it is looked in the next tile of the mask until a hit is found. If there is no hit in the mask region, no time-stamp is assigned to the track.

(a) Track geometry in rz-plane

(b) Track geometry in xy-plane

Figure 6.1.: Geometry of a track (red) in rz-plane **(a)** and xy-plane **(b)** with two layers of the pixel detector (green) and the tile detector (blue). The traveling path of a particle can be determined by the two angles θ and tan, the 3D-radius of the helix, and the latest known position. The stars indicate the hit information in the pixel and tile detector. Note that this sketch is not to scale.
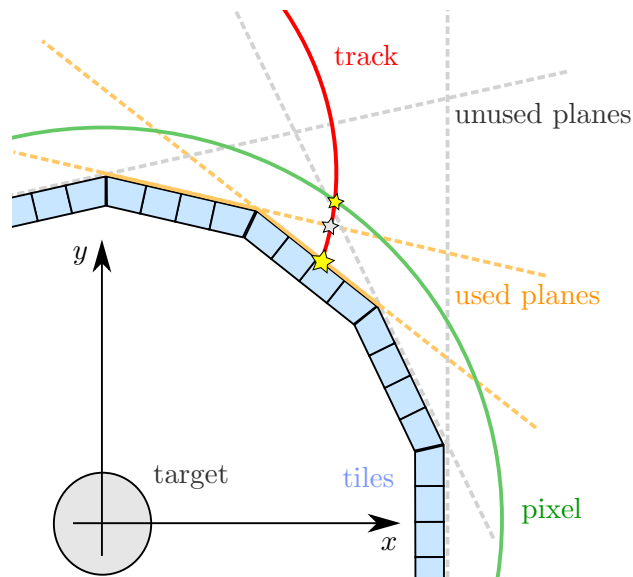

Figure 6.2.: Schematic view of a section of the detector to visualize the estimation of the impact position of a track on the tiles. Every edge of the tile detector defines a plane parallel to the beam-line (dashed lines). The two planes defined by the tiles that are nearest to the last hit in the pixel detector are used for predicting the impact position of the track on the tiles (orange). The intersection of the helical track with both planes is calculated. If the coordinates of one of those intersection points coincides with the position of the tiles (solid part of the orange lines), the predicted impact position is found. For simplicity the pixel detector is approximated as a circle and the drawing is not to scale.
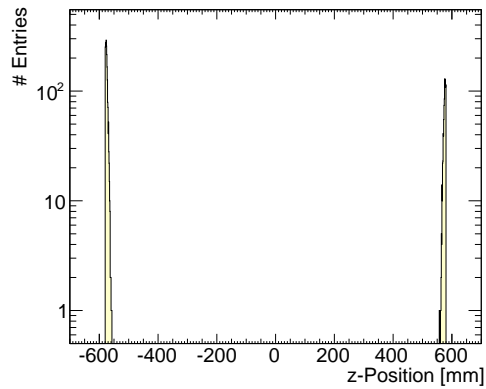
Figure 6.3.: z-Position in the last pixel layer of selected tracks that do not hit the tiles (phase 1 data set). These hits are all located at the end of the stations. Because of the alignment of the tiles with the pixel detector, and the momentum of tracks in z-direction, they are overshooting and thus missing the tile detector.
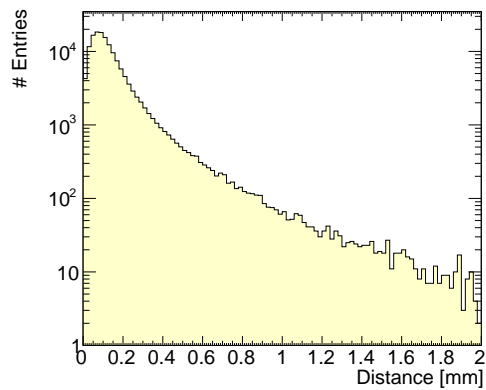

Figure 6.4.: Distance between the estimated impact of the track on the tiles and the true impact position (phase 1). The distribution quickly decreases after the maximum at 100 µm. This indicates the high precision of the estimate of the impact position. For phase 2 similar results are obtained.
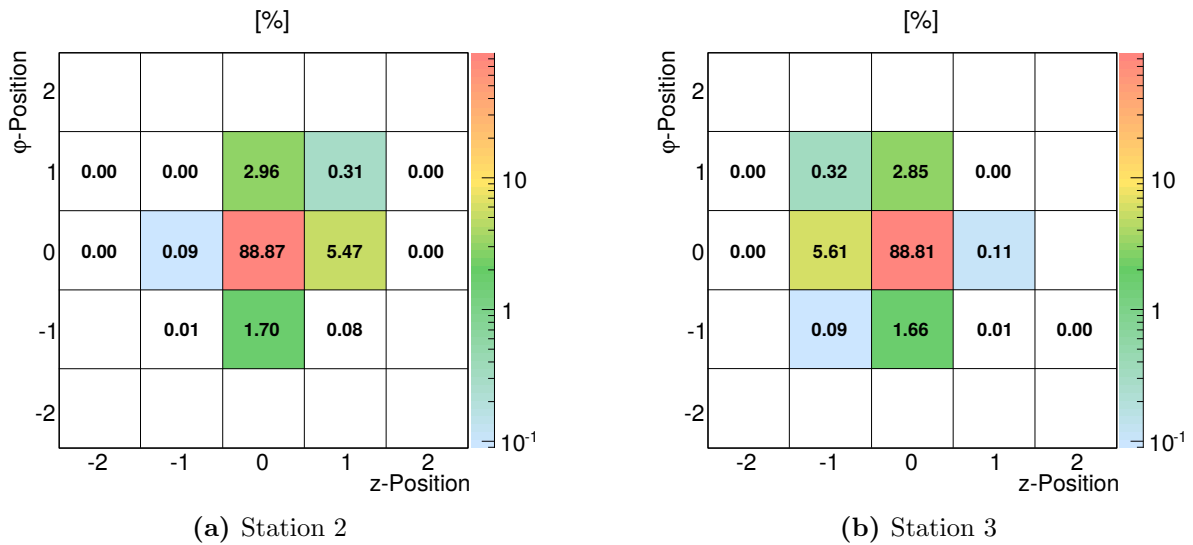
(a) Station 2

(b) Station 3

Figure 6.5.: Map of the relative position between the predicted tile of first impact and the true tile of first impact for station 2 **(a)** and station 3 **(b)** in a phase 1 setting. The detector is shown as a flat projection. The numbers are shown relative to the total number of estimated impact tiles. Over 88 % of the entries are located at position (0,0), which means that the estimated and the true tile of first impact are the same.

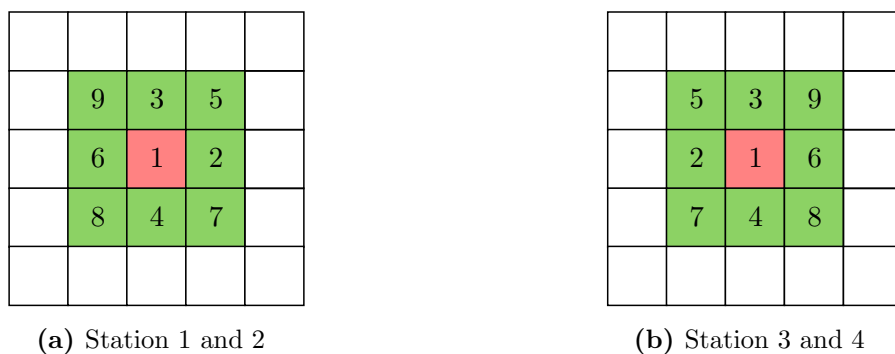**(a)** Station 1 and 2

(b) Station 3 and 4

Figure 6.6.: Mask to search for the best time-stamp of a track for stations 1 and 2 **(a)**, and stations 3 and 4 **(b)**. The red tile is the predicted tile of first impact. The numbers illustrate the order in which the tiles are searched for a hit. The order is determined by the probability profile of fig. 6.5.

41

The performance of the track-tile matching is summarized in table 6.1. For phase 1 99.54 % of the valid tracks are assigned with a time-stamp that is actually produced by this track. This number decreases to 93.68 % for phase 2. Because of the higher rate, more hits are lost due to pile-up and the probability of choosing a wrong hit increases. There are some hits that do not produce any hit in the tiles, despite their predicted intersection with the tiles. They are called *unmatchable*, because it is not possible to assign a time-stamp to those hits. A rough estimate of the influence of pile-up to the number of unmatchable tracks can be gained by the product of the mean pile-up (phase 1: 0.60 %; phase 2: 8.8 %) and the fraction of tracks producing only one hit in the tiles (39 %) giving 0.23 % for phase 1 and 3.4 % for phase 2. This is of the same order as the fraction of unmatchables given in table 6.1. Additional effects contributing to this are scattering in the last pixel layer with a large scattering angle and tracks hitting the tiles at the end of the station producing a too low energy deposition. Finally, matching errors are tracks that got an incorrect time-stamp, or none at all, even if the track produced a hit. This happens for 0.10 % of the tracks for phase 1 and 1.17 % for phase 2. The increase by a factor of ten for phase 2 is mainly due to the higher probability of assigning a wrong time-stamp to the track, due to the higher rate.

The causes for matching errors are listed in table 6.2. With 71 % for phase 1 (83 %, phase 2), the wrong assignment of ambiguous hits contributes most to the incorrect time-stamp assignment. For 29 % (16 %, phase 2), the true hit is out of the search region around the predicted tile. A bigger mask could lower this number, but would in turn increase the number of ambiguities.

Figure 6.7a and fig. 6.7b show the time difference between the assigned time-stamp and the true time of the track. The standard deviation of a gaussian fit to this distribution is a measure for the time resolution. This is determined to be 73 ps for both phases.

To further enhance the time resolution, the algorithm is extended by exploiting the fact that higher SiPM-signals are generating a more precise timing information (see section 3.5). The hit predicted by the procedure above is used as a reference hit. As discussed in section 5.3, hits are likely to be produced by the same particle, if they are in the same time window of 400 ps to the reference hit. Out of all hits that are located in the mask and are within the mentioned time window, the time-stamp of the hit with the highest energy deposition is being used. The time distribution of this procedure relative to the true hit is shown in fig. 6.7c and fig. 6.7d. This method enhances the time resolution by over 10 % to 64 ps for phase 1 and phase 2. However, it comes with the cost of a slight increase in matching errors. For phase 1 the matching error rises from 0.10 % to 0.13 % and for phase 2 from 1.01 % to 1.09 %.

Table 6.1.: Performance of the track-tile matching. Shown are the number of tracks that were assigned with a correct time-stamp, meaning a time-stamp produced by a hit from the same particle. The numbers in the column unmatchable include tracks that do not have a hit in the tiles even if the predicted impact position is on the tiles. The matching error is the number of events where no time-stamp could be found or the wrong time-stamp was chosen.

	Phase 1		Phase 2	
	Absolute	Relative	Absolute	Relative
Valid tracks	254,169	100.00 %	61,418	100.00 %
Correct matches	253,004	99.54 %	57,539	93.68 %
Unmatchable	924	0.36 %	3,261	5.31 %
Matching error	241	0.10 %	618	1.01 %

Table 6.2.: Reasons for an incorrect time-stamp assignment. Most errors occur by selecting a time-stamp generated by another track, while the correct one could have also been selected. For about 10 % of the mistakes done, the correct hit is out of range of the mask. Very rare (about 1 %) are events that have the correct hit in a different frame than the track is stored in.

	Phase 1		Phase 2	
	Absolute	Relative	Absolute	Relative
Matching error	241	100.0 %	618	100 %
True hit out of mask	69	28.6 %	100	16.2 %
Choosing wrong hit	170	70.5 %	510	82.5 %
True hit in wrong frame	2	0.8 %	8	1.3 %

(a) Phase 1

(b) Phase 2

(c) Phase 1, improved
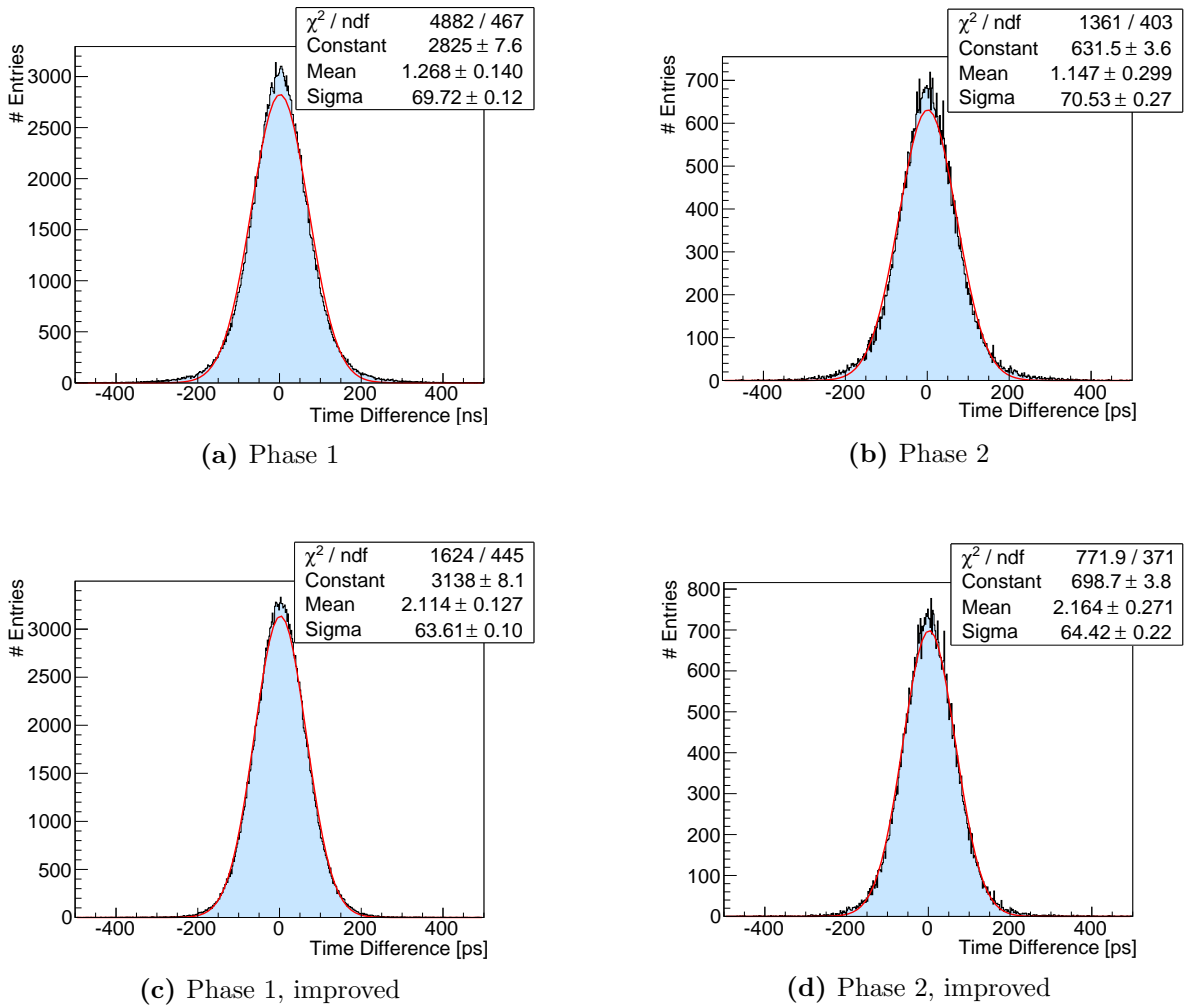
(d) Phase 2, improved

Figure 6.7.: (a),(b): Time difference of time-stamp assigned to a track and the true impact time of the track on the tiles. For both phases the width of this distribution is about 73 ps. **(c),(d):** Time difference between estimated and true time-stamp for the enhanced method. Besides an improvement of about 10 %, the distribution gets more gaussian.

6.4. Time Resolution of Signal Decays

In order to investigate the interaction of the track-tile matching with the track reconstruction, a data set with signal decays is analyzed. This data is produced with the signal branching ratio set to $\mathrm{BR}(\mu \rightarrow eee) = 1$ and a low rate of $2.5 \times 10^7\, \mu/\mathrm{s}$ for 200,000 frames, leading to 128,000 signal decays on the target. The vertex time is calculated for every track that hits the tile detector. The time of flight (TOF) of each particle is determined by the length of the track and subtracted from the time-stamp assigned by the track-tile matching. Because this study does not have an integrated vertex fit at the moment, the TOF of the trajectory is calculated between the first hit in the pixel layers and the last hit, and not from the vertex to the tile hit. This adds an uncertainty of about $2\,\mathrm{cm}$ (roughly the radius of the inner pixel layer) to the TOF calculation, corresponding to $\sigma_{\mathrm{TOF}} \approx 70\,\mathrm{ps}$.

The difference of vertex times should vanish for particles from the same signal vertex. The width of this distribution is determined by the uncertainty of the TOF calculation σ_{TOF} and the uncertainty of the time-stamp generated by the tiles $\sigma_{\mathrm{tiles}} = 63\,\mathrm{ps}$ (as determined above):

$$\sigma_{\mathrm{signal}}^{(\mathrm{theor.})} = \sqrt{\sigma_{\mathrm{TOF}}^2 + \sigma_{\mathrm{tiles}}^2} * \sqrt{2} \approx 130\,\mathrm{ps} \tag{6.1}$$

For the simulated data, the differences in the vertex time between events in the same frame are shown in fig. 6.8. A clear peak of particles produced at the same vertex can be distinguished from the background. The width of this distribution $\sigma_{\mathrm{signal}} = 123\,\mathrm{ps}$ is of the same order as the predicted resolution.

With an integrated vertex fit and an expected momentum resolution of $0.3\,\mathrm{MeV}$ for single tracks, the uncertainty of the TOF of the particles can be expected to be much less.
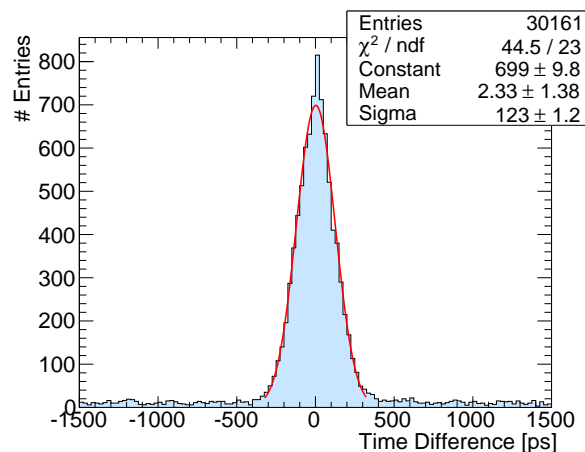

Figure 6.8.: Distribution of time differences of tracks that occur in the same frame for a data set with a signal branching ratio of $100\,\%$.

6.5. Possible Improvements

The main area for improvements may be at the solution of ambiguities, namely to find the right time-stamp between various hits in the region of the mask. Especially for phase 2 one may think of more advanced algorithms. The method presented above investigates each track separately. For cases where there are two or more hits from different tracks close in space and time, the right assignment of tracks to these hits might be improved by comparing the tracks last position and direction with the hits topology. A better dealing with ambiguities may also allow for bigger search masks around the predicted hit, increasing the sensitivity.

The algorithm presented above first predicts the impact position of the tracks and then searches for corresponding hits in the neighborhood. The reverse approach is to first cluster hits with the cluster reconstruction described in section 5.3 and than assign tracks to the cluster based on the topology of the cluster, which could lead to a decrease in mismatches of the track-tile matching.

Furthermore, the time information given by the fiber detector may help to lower the number of matching errors by reducing the size of the time window which is searched for suitable hits. Improvements in the computation time may be realized, if needed, by doing approximations. For example, a linear interpolation of the track instead of propagating the helix adds an uncertainty to the predicted impact position. However, due to the small distance between the pixel and the tile detector this effect plays a minor role and leads to a slight decrease in the number of correctly matched tracks of less than 0.1% for phase 1. The implementation of the linear interpolation in this study is about 10% faster than the helix propagation.

6.6. Conclusion

In this section an algorithm is proposed for the assignment of a time-stamp produced by the tile detector to the corresponding track, which is reconstructed by the pixel detector. The impact position of the particle on the tiles is predicted with an accuracy of $100\,\mu\text{m}$ by the geometry of the reconstructed track. The correct time-stamp is selected from the tiles in the close neighborhood of the impact position. The time resolution can be enhanced by about 10% if the time-stamp is selected from the hit with the highest energy deposition within a cluster. The proposed procedure assigns for 99.54% (phase 2: 93.68%) of the tracks a correct time-stamp to the corresponding track. In 0.10% (phase 2: 1.01%) of the tracks, a wrong time-stamp is assigned to the track. The missing percentages are unmatchable tracks, that have not produced a hit in the tile detector, mainly due to pile-up. These numbers are already a good starting point for further studies that may optimize the procedure; several suggestions for improvements are mentioned.

7. Time Calibration of the Mu3e Tile Detector

The timestamps generated in the readout electronics do not describe the exact time when the particle hits the tile surface, but the time when the SiPM-signal is processed by the readout electronics. This leads to an offset on the detection time for each tile, which depends on the wiring of the SiPMs to the chip (bond wiring and routing on the board) as well as on the synchronization of different chips and the configuration and manufacturing differences between the chips. These differences may be estimated prior to the construction in the laboratory with an uncertainty better than $1\,\mathrm{ns}$. Nevertheless, to achieve a precise time resolution of less than $100\,\mathrm{ps}$ for all channels, those differences have to be known precisely, which means a time calibration of the detector has to be performed. Because uncertainties in the calibration should not contribute significantly to the time resolution, the calibration has to be accurate up to $\mathcal{O}(10\,\mathrm{ps})$.

Temperature changes have influences on the conductibility of silicon and thus on the performance of the read-out chip. This may introduce differences on the detection times for different tiles. To account for this, the time needed for the calibration procedure should ideally be of the order of $10\,\mathrm{min}$, so that the detector can be quickly calibrated before every run.

A possible solution would be an LED-system with LEDs directly attached to the SiPMs which are flashing light simultaneously. However, such a system is not optimal, because it would increase the required space. A much better solution would be to use the muon decays in operation mode, so no extra construction would be needed.

The aim of this section is to investigate this possibility and to develop a calibration scheme. In order to test different approaches for a calibration in the simulation, a delay that is randomly drawn from a uniform distribution from $-50\,\mathrm{ns}$ to $50\,\mathrm{ns}$ is assigned to each tile. This delay is added to every time-stamp generated in the tile. The task of the calibration is to estimate this delay with high accuracy. In the following, various concepts for a time calibration of the Mu3e tile detector are studied.

7.1. Tools for the Calibration

Events that qualify for use in the time calibration of the tile detector should have several hits in different tiles, while the time distribution of those hits is precisely known. There are three event types fulfilling these requirements: Internal conversion decays, Bhabha scattering (that is scattering of a positron with an electron in the detector material) and particles hitting several neighboring tiles at once (i.e., clusters).

Using clusters for the calibration has the advantage of a very high rate, while direct calibration is only possible between neighbors and thus a calibration across stations is not possible. Using internal conversion decays or Bhabha events results in much lower rates, but the events are expected to be spread more widely over the detector. In the following, those processes and their feasibility for the calibration are described in detail. The discussion is based on a phase 1 setting with two recurl stations and a rate of $1 \times 10^8 \, \mu$ decays/s on the target. Each tile has to be calibrated relative to a certain *master-tile*. In order to achieve a precision of the calibration of 10 ps, about 100 events are required for each tile combination.

Feasibility Study of Using Clusters

As shown in section 5.3, about 60 % of particles hitting the tile detector are producing more than one hit in the tiles. About 45 % of events have a second hit in the direct neighbor tile in z-direction, while 13 % have a second hit in φ-direction. The tiles with the lowest rate at the end of station 3 have about 15,000 hits/s. This leads for every tile to more than 6,750 possible events per second in z- and more than 2,000 possible events per second in φ-direction which can be used for the calibration. This strongly recommends cluster events for a quick calibration with high precision.

However, two hits in adjacent tiles generated by the same particle are not happening at the same time, but the particle needs some time to travel to the second tile. The time of flight (TOF) can be estimated by having a look at the geometry as shown in fig. 7.1. Assuming a mean incident angle of $\alpha = 38°$ in z- and $\beta = 19°$ in φ-direction (see [13]), the mean TOF of the particle between the tiles for the current design (tile thickness $l_r = 5\,\text{mm}$, length in z-direction $l_z = 6\,\text{mm}$) can be estimated as:

$$\text{TOF}^{(\text{tile},z)} \approx \frac{d^{(\text{tile},z)}}{c} \approx \frac{l_r}{2\,c} \left(1 + \tan^2 \alpha + \tan^2 \beta\right) \approx 11\,\text{ps}, \tag{7.1}$$

$$\text{TOF}^{(\text{tile},\varphi)} \approx \frac{d^{(\text{tile},\varphi)}}{c} \approx \frac{d^{(\text{tile},z)}}{c} \left(1 - \frac{1}{3}\frac{l_r}{l_z} \tan \alpha\right) \approx 9\,\text{ps}. \tag{7.2}$$

Here, $\text{TOF}^{(\text{tile},z)}$ and $\text{TOF}^{(\text{tile},\varphi)}$ denote the mean TOF of the particles that hit another tile in z-direction or φ-direction, respectively. Further, $d^{(\text{tile},z/\varphi)}$ corresponds to the traveled distance
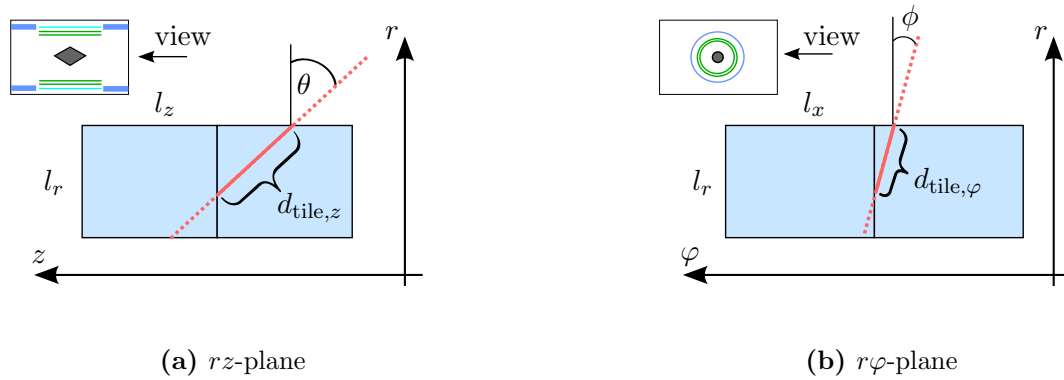
(a) rz-plane

(b) $r\varphi$-plane

Figure 7.1.: Geometry for particles (red) hitting two tiles in z-direction **(a)** and φ-direction **(b)**. Depending on the impact position and the incident angle, the distance d_{tile} traveled in the first tile and thus the time difference between the signals differs for the two tiles.

in the tile. The precise knowledge of the TOF of a particle between two tile hits is essential in order to minimize systematic errors of the calibration with clusters.

Feasibility Study of Using Internal Conversion Decays

Contrary to cluster events, internal conversion decays (ICs) have the advantage of producing hits everywhere in the detector and not only between adjacent tiles. This allows for a global calibration where different tiles positioned far away from each other are involved in the calibration of a tile. This is expected to be more robust against systematic errors than the calibration between neighbors as discussed above. At a first glance, ICs seem to be a good candidate for calibrating the detector. There are up to three hits from the same vertex and thus it is possible to determine the time difference between the signals in different tiles. However, with a branching ratio of $\mathrm{BR}(\mu \rightarrow eee\nu\nu) = 3 \times 10^{-5}$, it is questionable if there are enough events for the calibration of 6720 tiles (13,440 for phase 2, respectively). This will be investigated in the following.

The direct approach to calibrate a tile i relative to a fixed master-tile m is to use IC events that have hits in both tiles. The estimate for the delay $D^{\mathrm{est.}}_{m,i}$ between both tiles is the mean value of the time differences between both tiles:

$$D^{\mathrm{est.}}_{m,i} = \overline{dt}_{m,i} \equiv \overline{(t_m - t_i)}. \tag{7.3}$$

However, this method does not exploit the full information available. For example, the measurement of the time difference $\overline{dt}_{i,j}$ between tile $i \neq m$ and $j \neq m$ is not used. This

information can be included by calculating the delay as follows:

$$D^{\text{est.}}_{m,i} = \frac{1}{n-1} \left[\overline{dt}_{m,i} + \sum_{j=0;\, j \neq m,i}^{j=n} \left(\overline{dt}_{m,j} - \overline{dt}_{i,j} \right) \right], \tag{7.4}$$

where n is the number of tiles in a station and it is assumed that there is a hit $\overline{dt}_{i,j}$ for all i and j with $i \neq j$. In addition to the direct calibration term $\overline{dt}_{m,i}$, the terms $\left(\overline{dt}_{m,j} - \overline{dt}_{i,j} \right)$ include additional measurements and thus lead to a more efficient calibration procedure. This is illustrated in fig. 7.2.

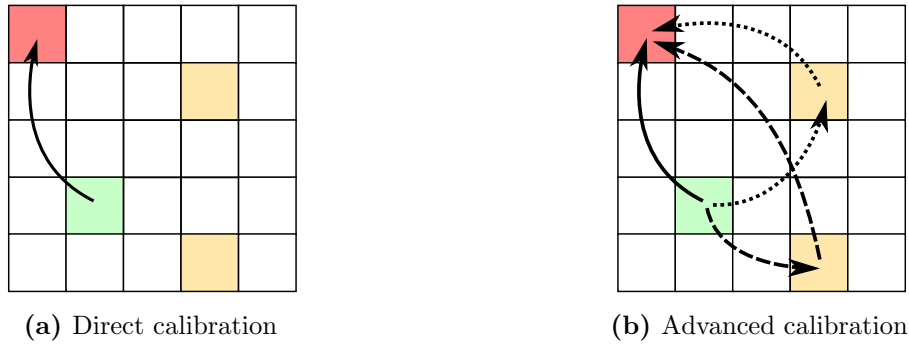**(a)** Direct calibration   **(b)** Advanced calibration

Figure 7.2.: Comparison of the direct calibration and the advanced calibration. Only using the direct information (solid line) to calibrate a tile (green) to a master-tile (red) **(a)** would not make use of the additional information given by the orange tiles. The advanced method also includes this information in the calibration procedure **(b)**.

In order to estimate the number of internal conversion events required for a calibration, it is assumed that there are in total N_p pairs of tile hits produced by one IC event. Further it is assumed that those pairs are equally distributed over the detector with $n = 6720$ tiles for two stations. The probability of an IC pair hitting tile m and tile i is:

$$P(m,i) = \frac{1}{n(n-1)}. \tag{7.5}$$

The expected number of IC pairs that contribute to $\overline{dt}_{m,i}$ is thus given by:

$$\hat{N}\left[\overline{dt}_{m,i} \right] = 2N_P * P(m,i) = \frac{2N_p}{n(n-1)}. \tag{7.6}$$

In this notation, $\hat{N}[X]$ denotes the expected number of IC pairs contributing to X. The factor 2 takes into account the fact that the first hit may be either in the master-tile or in tile i, hence giving two possibilities. For the term $\left(\overline{dt}_{m,j} - \overline{dt}_{i,j} \right)$, the expected number of IC pairs for a certain tile j can be calculated as:

$$\hat{N}\left[\overline{dt}_{m,j} - \overline{dt}_{i,j} \right] = 2 * \frac{2N_p}{n(n-2)} \frac{2N_p}{n(n-2)}. \tag{7.7}$$

Combining both, the expected number of IC pairs for the estimate of the delay between two tiles can be determined:

$$\hat{N}\left[D^{\text{est.}}_{m,i}\right] = \hat{N}\left[\overline{dt}_{m,i}\right] + (n-2) * \hat{N}\left[\overline{dt}_{m,j} - \overline{dt}_{i,j}\right] \tag{7.8}$$

$$= \frac{2N_p}{n\,(n-1)} + (n-2) * \frac{8N_p^2}{n^2(n-2)^2} \tag{7.9}$$

$$\overset{n\gg1}{\approx} \frac{2N_p}{n^2} + \frac{8N_p^2}{n^3}. \tag{7.10}$$

For the calibration this should be at least 100:

$$\hat{N}\left[D^{\text{est.}}_{m,i}\right] \overset{!}{=} 100. \tag{7.11}$$

Solving this equation for N_p leads to the required number of IC pairs:

$$N_p \approx n\sqrt{\frac{100}{8}n} \approx 1.9 \times 10^6. \tag{7.12}$$

The number of IC pairs in the experiment can be calculated with the IC branching ratio and the muon rate:

$$\text{BR}(\mu \to eee\nu\nu) * \text{Rate}(\mu) = 3 \times 10^{-5}\,\text{IC}/\mu * 1 \times 10^8\,\mu/\text{s} = 3000\,\text{IC/s}. \tag{7.13}$$

Because every IC event produces three primary electrons, there are three possible combinations of electron pairs for each IC event. This leads to 9000 IC pairs/s. If all of them could be used for the calibration, it would take about 4 min to reach the required calibration precision.

As shown in section 5.4 there are some constraints on the momentum of particles that may reach the tile detector. The transverse momentum has to be at least $p_T > 13\,\text{MeV}$ and the momentum in z-direction has to be $p_z > 10\,\text{MeV}$. It is observed, that particles hitting the tile detector have a total momentum of $p > 20\,\text{MeV}$.

Figure 7.3 shows the kinematic spectra in the simulation of the electrons produced in IC events. For this study a data set was generated using the simulation with the branching ratio of internal conversion decays set to 100 %, a muon rate on target of $1 \times 10^7\,\text{Hz}$ and 100,000 simulated frames, resulting in about 50,000 decaying muons on the target.

The results are well in agreement with those found in [42]. The total energy of all three charged leptons starts to rise at 20 MeV with a hard cut-off at 53 MeV (see fig. 7.3d). As can be seen in fig. 7.3b, the momentum of the electrons peaks at a few MeV. The distribution of the positron momentum, as shown in fig. 7.3a, is shifted to higher energies compared to the electron spectrum, thus it is more likely to get a high momentum positrons from an IC decay. However, fig. 7.3c shows that the momentum difference between the two positrons is large with a high probability. In this case one positron carries most of the momentum, while the other has a low momentum.
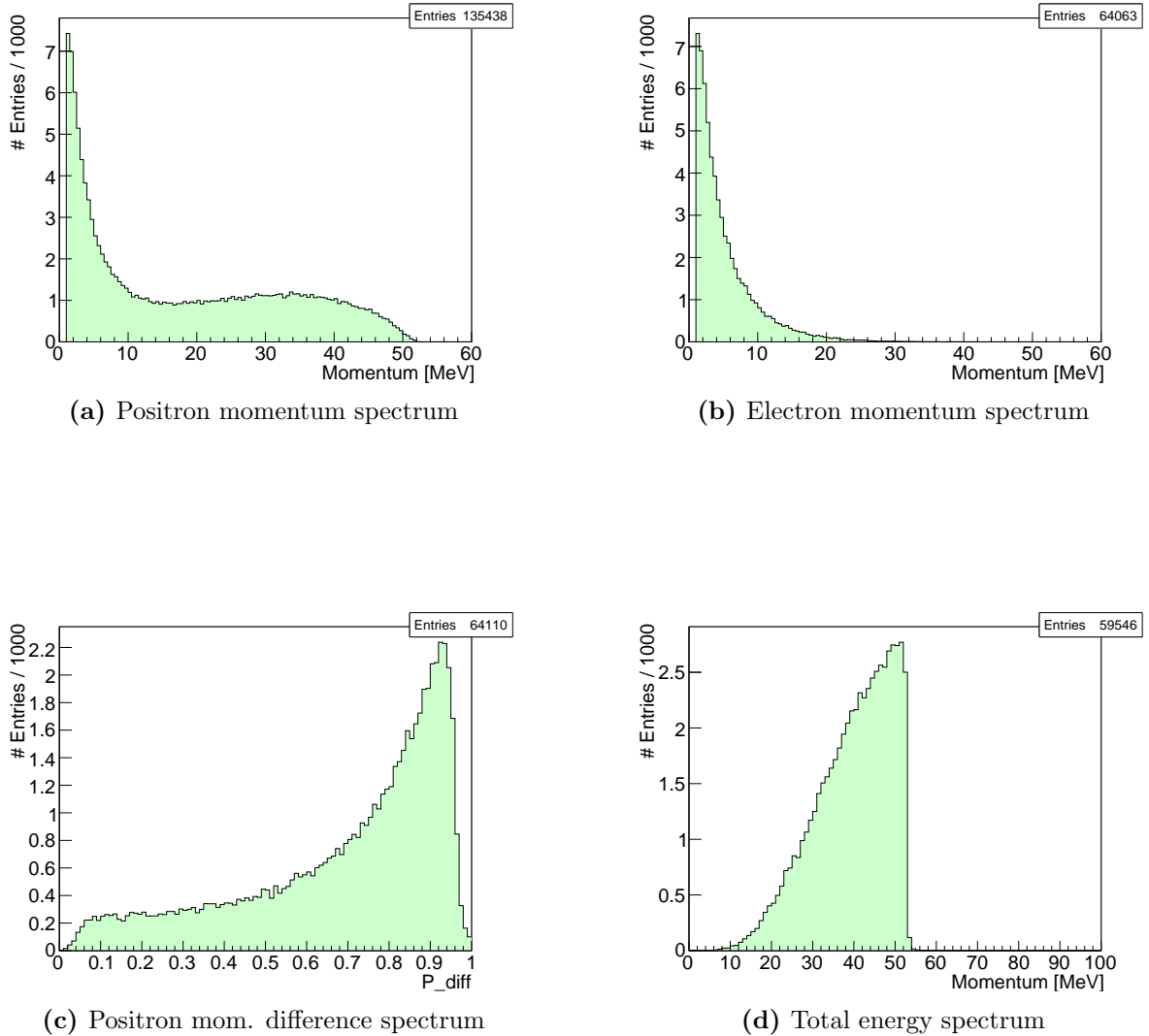
(a) Positron momentum spectrum

(b) Electron momentum spectrum

(c) Positron mom. difference spectrum

(d) Total energy spectrum

Figure 7.3.: Spectra of products of internal conversion decays in the simulation. **(a)**,**(b)** Distribution of the positron (electron) momentum. **(c)** Distribution of $P_{diff} = |\vec{p_1} - \vec{p_2}|/|\vec{p_1} + \vec{p_2}|$, i.e., the difference of the momentum of the positrons from the same IC event. A value of $P_{diff} \approx 1$ means that one positron carries nearly all momentum, while for $P_{diff} = 0$ the momenta of both positrons are equal. **(d)** Total energy spectrum of all three charged leptons of an IC decay. The data set excludes particles with a momentum of less than 1 MeV.

To further analyze how many pairs of charged leptons are coming from the same IC vertex and are able to reach the tiles, the momentum correlation of the decay products is shown in fig. 7.4. The momenta of two charged leptons from one IC event are anti-correlated to each other (figs. 7.4a and 7.4b), while the momenta in z-direction (p_z) are proportional (figs. 7.4c and 7.4d). This means that IC events are not suited for inter station calibration, because the two high momentum particles are likely to travel in the same direction and thus hitting the same station. In addition to the arguments given above, it can be seen that a pair of charged leptons from the same IC both hitting the tiles is rare. Figure 7.5 shows the fraction of charged lepton pairs from the same IC as a function of a cut on p_z. For a cut of $p_z > 10\,\text{MeV}$ there are only about 100 pairs left.

Out of the 150,000 pairs of particles from one IC decay, there are 60 pairs of hits found in the tiles that were generated by two particles from the same vertex. After running the track-tile matching, there are 7 pairs of tile hits left with a matching track. The other pairs of tile hits were produced by tracks that are not in the acceptance of the outer layers of the pixel detector. All of the 7 pairs have both hits in the same station. The number of generated IC events corresponds to about 17 s of phase 1b data taking. This means that there are about 25 pairs/min in the tiles from the same vertex usable for the calibration of the tile detector, which is by far not enough for a calibration with the required precision.

### Feasibility Study of Using Bhabha Scattering Events

The scattering of a positron on an electron is known as *Bhabha scattering* [43]. Currently, the kinematics of Bhabha scattering are not fully implemented in the simulation. Thus a detailed study as above for ICs events is not possible. However, a few thoughts on Bhabha scattering events will be presented here, mostly based on studies by N. Berger [44].

It was observed, that the probability of Bhabha scattering in the target region is 5.7×10^{-5} per muon decay in the simulation. For phase 1, this corresponds to 570 e^+/e^- pairs per second. Bhabha scattering may also happen at the pixel layer or the support structure. However, this discussion is focused on Bhabha events that originate from the target.

Because of energy and momentum conservation, the initial positron has a maximum momentum of 53 MeV. Both particles need a momentum larger than 20 MeV to reach the tile detector. Thus, the momentum of the initial positron has to be near the maximum of 53 MeV. Additionally, the scattered particles have to share the initial momentum approximately equally and the momentum in z-direction has to be sufficiently high to reach the tile detector. However, it was shown in the simulation that the momentum of the scattered electron favors low momenta. Therefore the probability for both particles of a Bhabha pair hitting the tile detector is unlikely to exceed a few percent. This would lead to at most 10 Bahbha pairs in the tile detector per second. Despite the qualitative nature of this discussion, it can be stated, that it is not likely that a fast calibration of the tile detector with Bhabha events is feasible. However, there might be more Bhabha pairs in the detector than IC pairs.
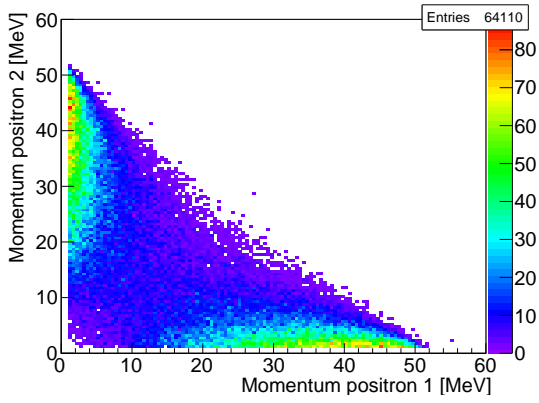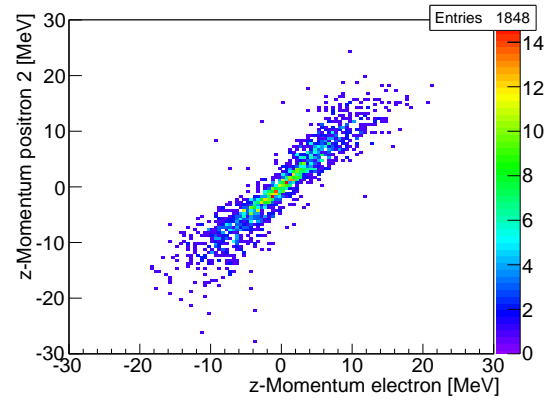
(a) Corr. of positron momenta
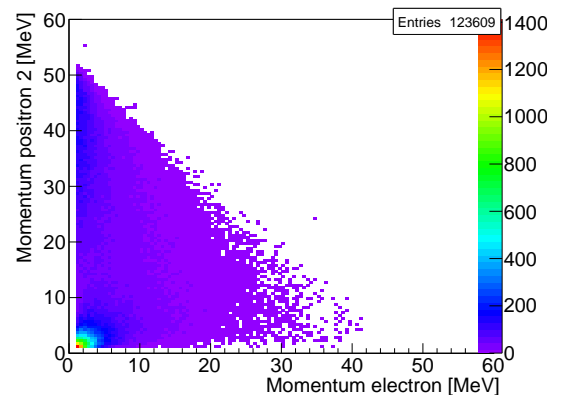
(b) Corr. of positron/electron momenta
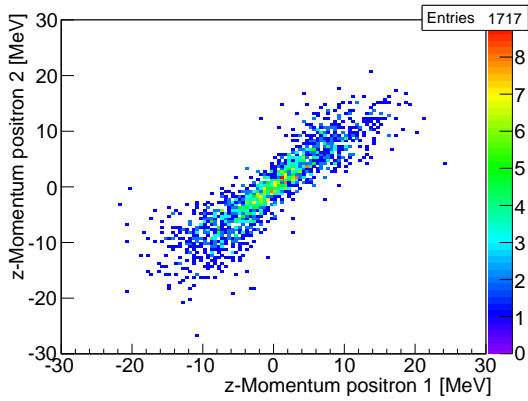
(c) Corr. of positron z-momenta

(d) Corr. of positron/electron z-momenta

Figure 7.4.: Correlation of the momenta of a positron and **(a)** an electron or **(b)** the second positron from one IC decay. Figs. **(c)** and **(d)** show the momenta in z-direction, respectively.
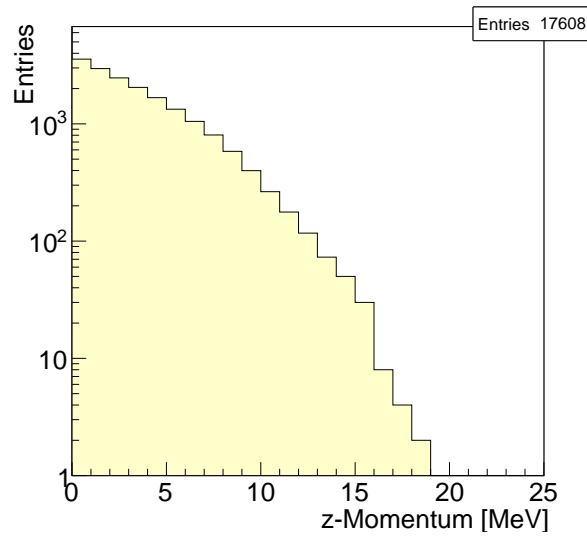
Figure 7.5.: Number of pairs from the same IC vertex passing a cut on the z-momentum for both particles. Additionally the two particles are required to have a transverse momentum of more than $13\,\mathrm{MeV}$.

Conclusions

The presented studies show that internal conversion decays are not suitable to calibrate the tile detector of the Mu3e experiment on a short time scale. Besides the expected rate of about 9000 IC events per second, very few coincident hits in the tile detector for two electrons from the same vertex are observed, which is due to the kinematics. For most cases, one electron carries most of the momentum, while the other two electrons have low momenta and do not reach the tiles.

For Bhabha events, no final statement can be given due to the lack of an implementation of the kinematics in the simulation. However, the discussions above suggest that the number of e^+/e^- pairs in the tile detector might be higher than the number of pairs from the same IC event. Nevertheless, it is not expected to observe a rate high enough for a fast calibration of the tile detector.

Cluster events showed to be the most promising tool for the calibration. A rate of a few thousand events per second even for the tiles at the end of station 3 give enough statistics for a fast calibration. However, one problem remains: Cluster events can only be used to calibrate between adjacent tiles and might be prone to potentially large systematic errors. In the following, this problem is addressed and a procedure is presented to calibrate the tile detector using cluster events.

7.2. Cluster Calibration

As discussed above, cluster events are highly suitable for the time calibrating of stations. The clusters are selected as described in section 5.3 using the small mask (fig. 5.7a). For the calibration process, no constraint on the time difference between the hits can be determined, because the delay between the tiles is not known at the moment of the calibration.

In the following, the algorithm of the calibration of the tile detector with cluster events as well as its performance is presented. The cluster calibration consists of three steps. First, an estimate for the difference in delay between neighbors is calculated. Second, the rows in the z-direction of the tile detector are calibrated relative to a *row-master-tile*. Finally, the whole station is calibrated to a *station-master-tile*. For this analysis, a data set is used with 1,000,000 frames of phase 1 rate ($1 \times 10^8 \, \mu$ on target/s), corresponding to $50 \, \text{ms}$ of data.

Calibration of Neighbors

By comparing the time difference of two tile hits in one cluster event, the delay between both tiles can be estimated. Because of mis-reconstuction some tile hits in a cluster might not be generated by the same particle and are thus be considered as noise. The time difference of those two mis-reconstructed particles may be as large as the time window of 1 frame ($50 \, \text{ns}$) and thus introducing a large error in the estimation of the delay. These outliers are reduced by calculating the median of all data points for one tile combination. Events are rejected if they are more than $500 \, \text{ps}$ away from the median. This procedure is illustrated for two neighboring tiles in fig. 7.6. For phase 1, $1.6 \, \%$ of the hit pairs are reject.

After the noise reduction, the mean value $\overline{dt}_{i,j} = \overline{(t_i - t_j)}$ of all time differences for hits in one cluster between two tiles i and j is calculated. This is used as an estimate for the delay $D_{i,j}^{\text{est.}}$ between the two tiles i and j:

$$D_{i,j}^{\text{est.}} = \overline{dt}_{i,j}. \tag{7.14}$$

The error on the estimated time difference between two tiles i and j is defined as

$$\Delta D_{ij} \equiv D_{i,j}^{\text{est.}} - D_{i,j}^{\text{truth}}, \tag{7.15}$$

where $D_{i,j}^{\text{est.}}$ is the estimated delay and $D_{i,j}^{\text{truth}}$ is the true delay. The distribution of the error $\Delta D_{i,j}^{(z)}$ and $\Delta D_{i,j}^{(\varphi)}$ for neighboring pairs in z- and φ-direction is shown in fig. 7.7. For both distributions, the mean is shifted to $\mu_{\Delta D}^{(z)} = 12.7 \, \text{ps}$ and $\mu_{\Delta D}^{(\varphi)} = 7.1 \, \text{ps}$. This is due to the already mentioned TOF of the particle. The rough estimate of this effect, as shown in section 7.1 predicts similar values. The width of the two distributions is $\sigma_{\Delta D}^{(z)} = 6.4 \, \text{ps}$ and $\sigma_{\Delta D}^{(\varphi)} = 11.7 \, \text{ps}$. There is a larger uncertainty on the estimated delay for neighbors in φ-direction, because there are nearly 4 times less events than in z-direction. This corresponds to a $\sqrt{4}$ times worse resolution.
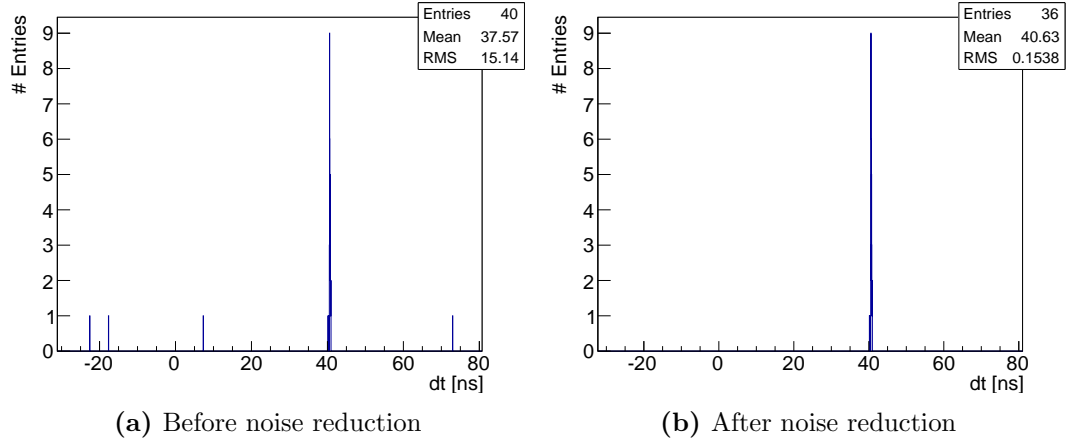
(a) Before noise reduction   **(b)** After noise reduction

Figure 7.6.: Time difference of clustered hits for two neighboring tiles before **(a)** and after **(b)** the noise reduction. The four outlier hits are rejected while all hits in a 500 ps time window around the median are retained.
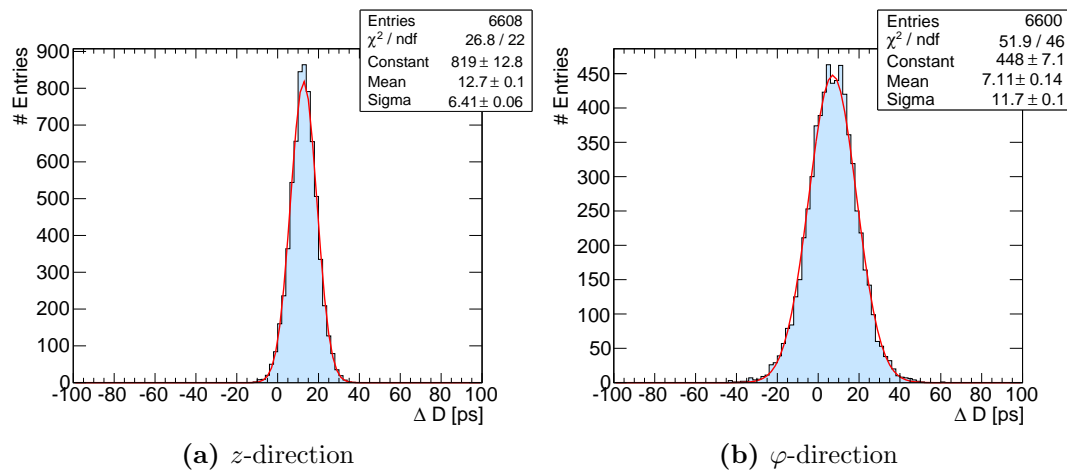

(a) z-direction   **(b)** φ-direction

Figure 7.7.: Distribution of $\Delta D_{ij} = D_{i,j}^{\text{est.}} - D_{i,j}^{\text{truth}}$, which is the difference between the estimated delay and the true delay for two neighboring tiles. **(a)** For neighboring tiles in z-direction, **(b)** for neighboring tiles in φ-direction.

Calibration of Rows

By using cluster events with the second hit in z-direction, every tile on a certain row in z-direction is calibrated to its row-master-tile, defined as the tile nearest to the target for every row. Because of the shift of the distributions in fig. 7.7, a term $\text{TOF}_{i,j}$ accounting for the time of flight of the particle between two adjacent tiles i and j is added to the estimation of the delay $D_{i,j}^{\text{est.}}$ between both tiles:

$$D_{i,j}^{\text{est.}} = \overline{(t_i - t_j)} + \text{TOF}_{i,j} = \overline{dt}_{i,j} + \text{TOF}_{i,j}, \tag{7.16}$$

where t_i and t_j are the measured time-stamps of the two tiles.

As depicted in fig. 7.8a, all tiles in a row are iteratively calibrated to the row-master-tile m in the following way:

$$D_{m,k}^{\text{est.}} = D_{m,k-1}^{\text{est.}} + \overline{dt}_{k-1,k} + \text{TOF}_{k-1,k}. \tag{7.17}$$

If the last tile of the row is reached, an estimate for the delay between every tile to its row-master-tile can be stated. This procedure equals a gaussian random walk. Thus, the uncertainty on the estimate of the delay between the row-master-tile and a tile at position $n_z = 59$ is given by $\sigma_{\Delta D}^{(z)} * \sqrt{n_z}$. Therefore, the last tile in the row has an uncertainty on the estimation of the delay to the row-master of $\sigma_{\Delta D}^{(z)} * \sqrt{59} = 49\,\text{ps}$. The error $\Delta D^{(\text{row})}$ on the estimate of the delay between each tile and its row-master-tile compared with the true value is shown in fig. 7.8b. This is corrected for the systematic error due to the TOF of the particles to the neighbor tile, which is estimated from fig. 7.7a and assumed to be known precisely for now. As expected, the distribution is not gaussian, but rather an overlay of 59 gaussian distributions with an increasing width. However, the width of the gaussian fit to this distribution gives a good estimate for the uncertainty of the row calibration. This width is $\sigma_{\Delta D}^{(\text{row})} = 21\,\text{ps}$. Figure 7.9 shows the same values in a map according to the position on the detector of each tile. The random walk behavior from the left side to the right side for each row can be clearly seen.

Calibration of Stations

To calibrate every tile on a station relative to a station-master-tile M, the rows have to be calibrated with each other. The scheme for doing this is similar to the method used above and is depicted in fig. 7.10a. Because the tiles in a row are already calibrated relative to the row-master, the delay $D_{m_i,m_{i+1}}^{(\text{est.})}$ between the row-masters m_i and m_{i+1} of adjacent rows has to be estimated. For this, cluster events in φ-direction are used. In order to achieve a higher accuracy, not only the direct time information $\overline{dt}_{m_i,m_{i+1}}$ between both row-master-tiles is used, but also the time information $\overline{dt}_{k_i,k_{i+1}}$ between the other tiles in the row and their
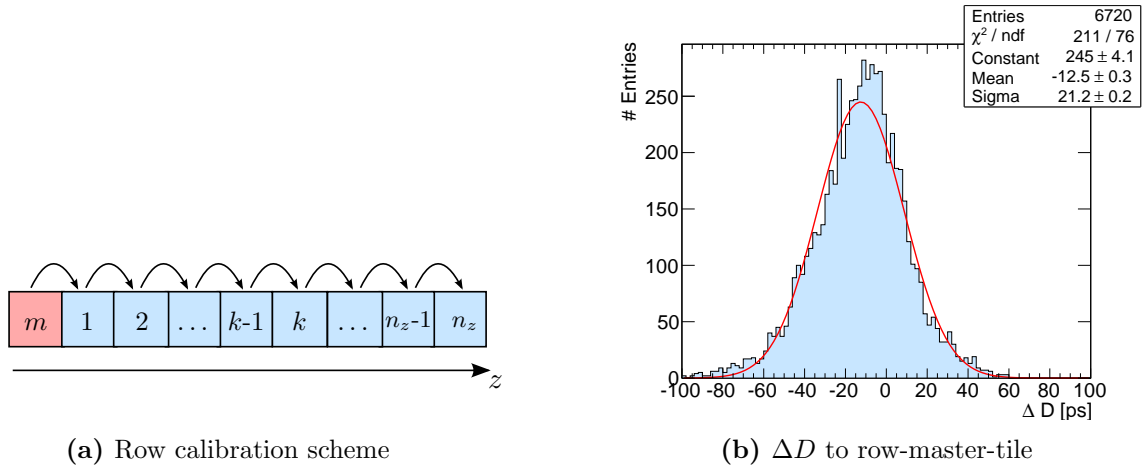
(a) Row calibration scheme

(b) ΔD to row-master-tile

Figure 7.8.: **(a)** Calibration scheme for calibrating a row relative to a row-master-tile m (red) in z-direction with cluster events. The estimated delay between the tiles is propagated through the row. **(b)** Distribution of the error $\Delta D^{(\mathrm{row})}$ on the estimated delay between each tile and the row-master-tile.
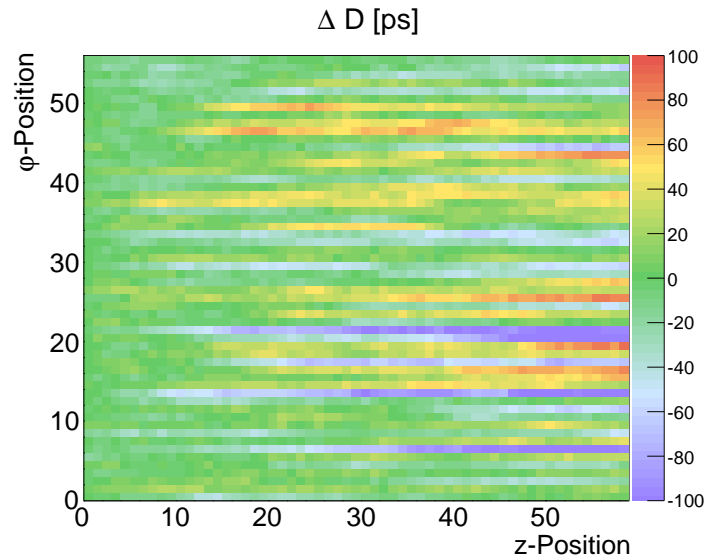

Figure 7.9.: $\Delta D^{(\mathrm{row})}$, i.e., the error on the estimated delay between each tile and its row-master. The x-axis shows the z-position, while the y-axis indicates the φ-position of the corresponding tile. The row-master-tiles are for each row at z-position $= 0$. The row-calibration follows a random walk. Thus the error on the estimated delay is much larger at the end of the row.

corresponding tiles in the adjacent row:

$$D^{\text{est.}}_{m_i,m_{i+1}} = \frac{1}{60} \left[\overline{dt}_{m_i,m_{i+1}} + \sum_{k=1}^{k=60} \left(D^{\text{est.}}_{m_i,k_i} + \overline{dt}_{k_i,k_{i+1}} - D^{\text{est.}}_{m_{i+1},k_{i+1}} \right) \right],$$ (7.18)

where, the subscript k_i denotes the kth tile in the ith row. The delay estimation of adjacent row-master-tiles is propagated around the ring in φ-direction until there is an estimate of the delay for every row-master-tile relative to the station-master. At the end of this procedure, an estimate of the difference of the delay between every tile in a station and the station-master-tile can be stated. The distribution of the difference $\Delta D^{(\text{station})}$ between the true and the estimated delay between every tile and the station master is shown in fig. 7.10b. The width of this distribution is $\sigma^{(\text{station})}_{\Delta D} = 18\,\text{ps}$ and the mean is shifted by about $-10\,\text{ps}$. The shift is a statistical effect and will vanish for larger data sets. In any case, an offset is not a problem, since only the relative delays between the tiles are of interest.

Figure 7.11 shows the distribution of the error on the delay estimation $\Delta D^{(\text{station})}$ over the detector for station 2. Compared to fig. 7.9, the uncertainties are smaller, because of the averaging done in eq. (7.18). The tiles with the largest deviation from the true delay are distributed at the edge of the detector, which is a result of the random walk behavior.

Figure 7.12 shows the uncertainty of the calibration over the calibration time T. For the first 30 ms, the uncertainty of the calibration is proportional to $\frac{1}{\sqrt{T}}$, indicating, that the uncertainty is limited by statistics. For calibration times longer than 30 ms, the precision of the calibration does not increase significantly. This is due to the systematic error on the TOF of the particles between the tiles, which will be addressed in the following section.

Reducing the Systematic Error

For the analysis above the mean time of flight $\text{TOF}_{i,j}$ of the particles between two tiles i and j is assumed to be known, and was estimated using the distributions in fig. 7.7. However, in reality this may not be known that precise. Figure 7.13 shows the effect of a systematic error on the estimated TOF between the tiles. For a systematic error on $\text{TOF}_{i,j}$ of more than 1 ps the uncertainty of the calibration procedure increases linear by 24 ps per pico second. To reach a precision of the calibration of about 10 ps, the TOF of the particles has to be known with an accuracy of less than 1 ps.

For the studies above, the mean TOF of particles between two adjacent tiles are estimated from the distributions in figs. 7.7a and 7.7b. However, particles at the end of the station have a larger mean incident angle of $\theta \approx 50°$, while particles at the beginning of the station (i.e., near the target) have incident angles of $\theta \approx 30°$ [13]. This leads to differences on the TOF. A more precise estimation has to take this into account and assign a value for the TOF between the tiles individually to each track based on the incident angles and the impact position.
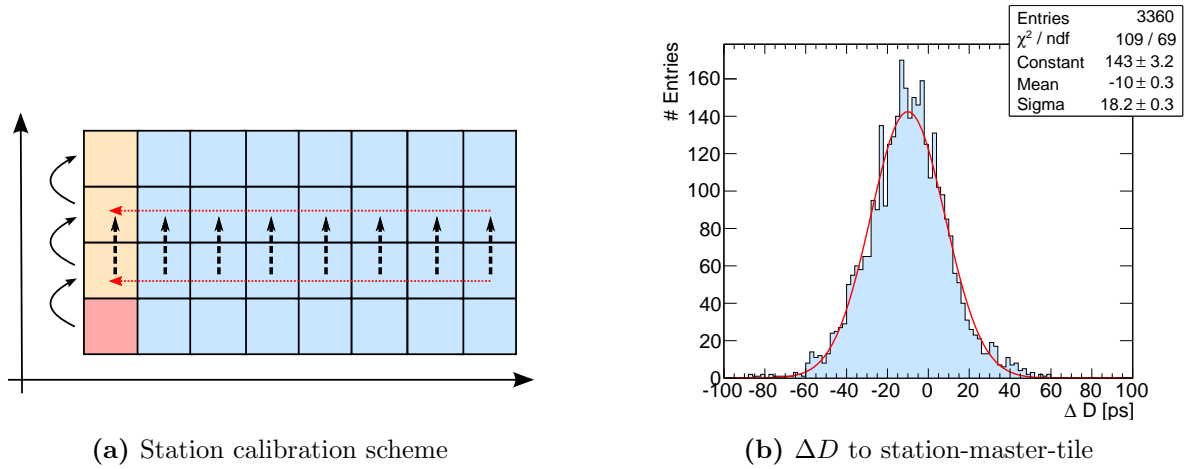
(a) Station calibration scheme   **(b)** ΔD to station-master-tile

Figure 7.10.: **(a)** Calibration scheme for calibrating a station relative to a station-master-tile (red) using cluster events in φ-direction. The estimated delay between the tiles is propagated through the columns of the detector. The delay of two adjacent rows is averaged using all tiles in the row. **(b)** Distribution of the error $\Delta D^{(\text{station})}$ on the estimated delay between each tile and the station-master-tile.
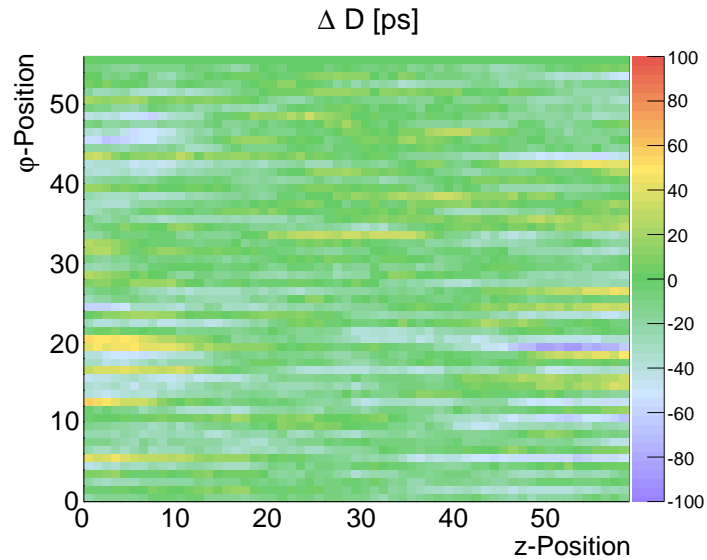
Figure 7.11.: $\Delta D^{(\text{station})}$, i.e., the error on the estimated delay between each tile and its station-master-tile for station 2. The x-axis shows the z-position, while the y-axis indicates the φ-position of the corresponding tile. The station-master-tile is at $z = 0$ and $\varphi = 0$.
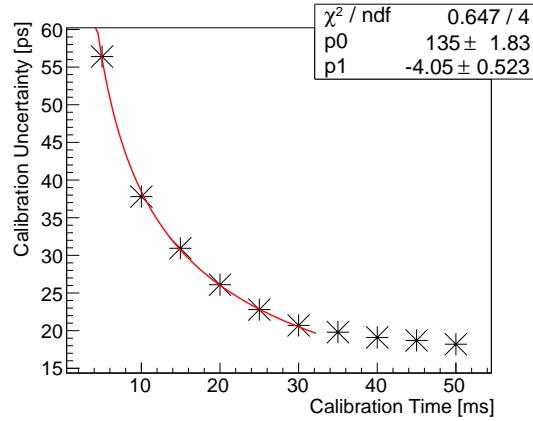
Figure 7.12.: Uncertainty of the calibration procedure over the calibration time. The function $p_0/\sqrt{x} + p_1$ is fitted on the data for calibration times less than 30 ms. The data follows the one over square root of n behavior as is expected for a statistical process. For calibration times over 30 ps, systematic errors dominate the uncertainty of the calibration.
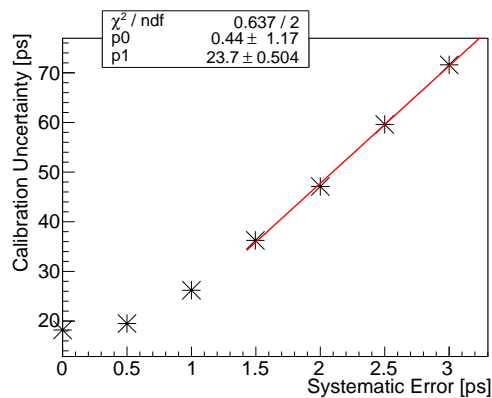

Figure 7.13.: Influence of a systematic error on the estimation of the TOF between two adjacent tiles on the precision of the calibration. For small systematic uncertainties of less than 0.5 ps, the precision of the calibration is dominated by the statistical uncertainty. Above a systematic error of 1.5 ps, the precision of the calibration is determined by the systematic uncertainty.

There are a variety of possibilities how to estimate the length of the path of the trajectory in the tiles. The detailed geometrical calculations may give a good estimation for this, especially for the dependence on the incident angle and the impact position.

Another approach is the use of particles from the same vertex, i.e., from IC events or Bhabha scattering. If one particle of the pair generates a hit at the beginning of the station and the other one produces a hit at the end of the station but within the same row, the systematic error can be estimated over a wide range of tiles. Because this is a systematic effect that is not expected to change significantly within the operation of the detector it has not to be as fast as the calibration procedure above. Due to the low rate of pairs from the same vertex, this method may take some time but could improve the precision of the calibration over time. However, it only gives an estimate for the average TOF of the particles and no information about the dependence on the incident angle or the impact position of the trajectory. A detailed Geant4 simulation of two tiles with a simulation of the photon propagation and generation in the scintillators or a direct measurement may also give predictions for the value of $\text{TOF}_{i,j}$. This is a crucial point in the calibration process and has to be addressed by further studies. Nevertheless, an estimation of the systematic errors with a precision of up to 1 ps seems feasible. This would allow for a calibration with the targeted precision using cluster events.

7.3. Inter Station Calibration

The final step of the calibration procedure is the calibration of the stations with each other, i.e., the *inter station calibration*. For this, events are required, that have hits in both stations with a known time distribution. As shown in section 7.1, the z-momentum of pairs of electrons from internal conversion events is correlated in a way, that both particles are likely to hit the same station. In 50,000 IC events, no pair was observed in the simulation to hit two tiles in different stations. Thus, IC events are not usable for the inter station calibration. With cluster events only adjacent tiles can be calibrated. Therefore, they can not be used either.

One possibility for the inter station calibration would be to use the fiber detector. The fiber detector is expected to have a time resolution of less than $1\,\mathrm{ns}$ and it assigns a time-stamp to each track. To reach a precision of $10\,\mathrm{ps}$ there are $(1\,\mathrm{ns}/0.01\,\mathrm{ns})^2 = 10000$ tracks required, which will be achieved in much less than a second of data taking. This procedure intrinsically calibrates the fiber detector with the tile detector. The delay $D^{\mathrm{est.}}_{s_i,\,\mathrm{fiber}}$ between one station s_i of the tile detector and the fiber detector is calculated as the mean value of all differences of the time-stamp of a hit in a tile station t_{s_i}, the time-stamp of the fiber detector t_{fiber}, and the TOF t_{TOF} of the particle between both detectors:

$$D^{\mathrm{est.}}_{s_i,\,\mathrm{fiber}} = \overline{(t_{s_i} - t_{\mathrm{fiber}} - t_{\mathrm{TOF}})}, \tag{7.19}$$

The estimated delay between the two stations is then given by:

$$D^{\mathrm{est.}}_{s_1,s_2} = D^{\mathrm{est.}}_{s_1,\,\mathrm{fiber}} - D^{\mathrm{est.}}_{s_2,\,\mathrm{fiber}}. \tag{7.20}$$

The track-fiber matching is currently work-in-progress and not integrated with the track-tile matching in the track reconstruction. Therefore, a detailed simulation study of this procedure is not possible. A short-coming with this method is that systematic uncertainties of the fiber detector, may degrade the calibration Furthermore, it is only possible to calibrate the stations by using information of the fiber detector if the fiber detector is working as intended. A calibration procedure that does not rely on another sub-detector would be more desirable. Another candidate for the calibration of stations with each other might be Bhabha scattering events. To investigate this possibility, further studies are needed.

Finally, a different approach is the use of extensive air showers (EAS), which are generated in the atmosphere by high energetic cosmic protons or heavier nuclei and have an electromagnetic, muonic and hadronic component [45]. They often contain more than one million particles and are distributed over a range of more than $100\,\mathrm{m}$ on the earth's surface. The duration of an EAS is of a few nano seconds [46]. If there are some of these events within a reasonable time, they may be used for the calibration of the stations. However, this has to be investigated in further studies.

7.4. Conclusion

The time calibration of the Mu3e tile detector is necessary to account for response differences between different channels. The calibration procedure is required to be accurate up to $\mathcal{O}\left(10\,\mathrm{ps}\right)$. Since temperature differences or radiation damage may influence the timing behavior of the detector, a fast calibration is desirable in order to calibrate the detector before every run. A calibration using events that occur during the normal operation mode of the detector is of special interest, because this would prevent an extra construction of a calibration system. This chapter explored possible calibration schemes that fulfill the requirements presented above.

IC events, Bhabha scattering and cluster events are possible candidates for a calibration. They have in common that all three event types produce multiple hits in the detector with a known time distribution. Thus the time differences between the hits can be used to estimate the delay between the different tiles. Despite the occurrence of about 9,000 IC pairs per second, a study on the kinematics of the decay products of these events shows, that only few of this events reach the tile detector. Most pairs have one particle with a too low p_z or p_T. For 50,000 simulated IC events, there are only 7 pairs with a matched track for which both particles produce hits in the tile detector. This corresponds to about 25 pairs/min. For a full calibration of the detector, about 2 million pairs would be needed. Thus, a fast calibration with IC events is not feasible.

Because the kinematics of Bhabha scattering are not implemented in the simulation at the moment, no clear statement can be given. However, it is expected that not all Bhabha scattering pairs can be used for the calibration and the number of usable pairs is of the same order as for the IC events.

Cluster events showed to be usable for a fast calibration with high precision. The expected rate is of a few thousand events per second. However, a shortcoming of cluster events is that the calibration is only possible between adjacent tiles. A scheme is presented how to use cluster events to calibrate a whole station. Using this method, a precision of less than 20 ps is achieved. For this result, it is assumed that the time of flight of a particle between two tiles is known with an uncertainty of less then 1 ps. The uncertainty of this value is crucial for the precision of the calibration. Various suggestions are given of how to estimate the time of flight between the tile hits with high precision.

Furthermore, suggestions for a calibration between the different stations of the tile detector are presented. However, this has to be analyzed in detail by further studies.

Conclusion

The Mu3e experiment aims at searching for the decay $\mu^+ \to e^+e^+e^-$, whith a sensitivity of 10^{-16}. Since this decay is predicted to be non-observable by the standard model of particle physics (SM), a measurement of the decay would directly imply new physics.

The tile detector is a sub-detector of the Mu3e experiment. The design goal of the tile detector is to provide a time-resolution of less than $100\,\mathrm{ps}$. It consists of a combination of scintillating tiles and silicon photomultipliers (SiPMs) detecting the scintillation light. In order to achieve the proposed time-resolution a time calibration of the detector has to be performed. The accuracy of the calibration should be much better than the expected time-resoultion.

This thesis presents a calibration scheme for the tile detector. For this, the track-tile matching, an important part of the event reconstruction, was developed. The track-tile matching solves the problem of the assignment of a time-stamp to a reconstructed track. The expected impact position of a particle track on the tiles is calculated by the parameters of that track given by the reconstruction. The time-stamp is selected from hits in the direct neighborhood of the expected impact position. The track-tile matching assigns the correct time-stamp with a probability of $99.54\,\%$ for a muon decay rate of 10^8 per second and $93.68\,\%$ for a rate of 10^9 per second. The percentage of wrong time-stamp for a track is $0.10\,\%$ for the lower rate and $1.01\,\%$ for the higher rate. The missing percentage are tracks that have not produced a time-stamp in the tile detector, mainly due to pile-up.

Different processes are studied for their feasibility of being usable in the calibration of the tile detector. Internal conversion decays ($\mu^+ \to e^+e^+e^-\bar{\nu}_\mu\nu_e$) are not suitable for the calibration. Because of the momentum distribution, only 25 electron pairs per minute from the same vertex are expected to hit the tile detector, which is by far not enough for a fast calibration. The most promising candidate for a calibration procedure are cluster events, produced by particles hitting more than one tile. Over $60\,\%$ of particles are generating more than one hit in the tile detector. In combination with the high rates at the Mu3e experiment, sufficient statistics for the calibration can be gained by analyzing cluster events in under a second of data taking.

A calibration scheme for the relative time calibration of the tile detector is presented. Adjacent tiles are calibrated to each other by using the time information of cluster events. The calibration procedure is thus propagated through a complete station. A precision of the calibration of less than $20\,\mathrm{ps}$, which is already in range of the targeted precision of about $10\,\mathrm{ps}$ was achieved, using $50\,\mathrm{ms}$ of simulated data. It was shown that the precision of the calibration procedure is dominated by systematic errors, which are mainly given by the time of flight of a particle between two tiles. Various methods were proposed to reduce this systematics.

Part III.

Appendices

A. Cluster Maps (Phase 2)
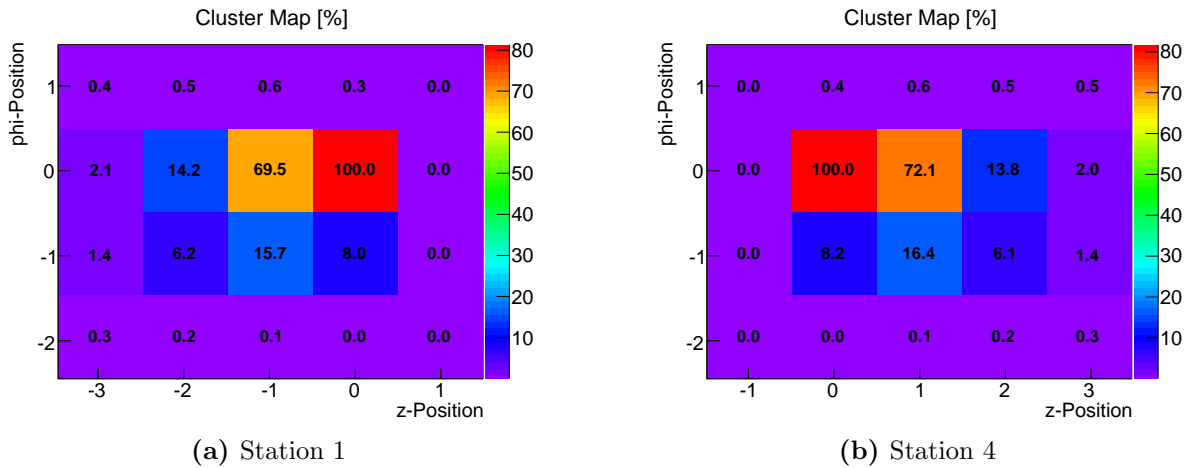

(a) Station 1

(b) Station 4

Figure A.1.: Cluster maps for all four stations with a phase 2 setting. The detector is rolled out. The first hit of a cluster is filled to the position (0,0) on the map. The other bins are filled with the corresponding fraction of hits relative to the first hit. Station 2 and 3 are similar to the results for the phase 1 settings in section 5.3. Nevertheless, station 2 has a few hits less in the second tile in z-direction compared to station 3, which is due to the higher rate and thus, a higher probability for pile-up. The outer stations 1 and 4 have a significantly higher contribution of particles also hitting the next tile, because the incident angle of the particles has to be smaller to reach those stations.

B. True Tile of First Impact Relative to Estimated Tile (Phase 2)

(a) Station 1
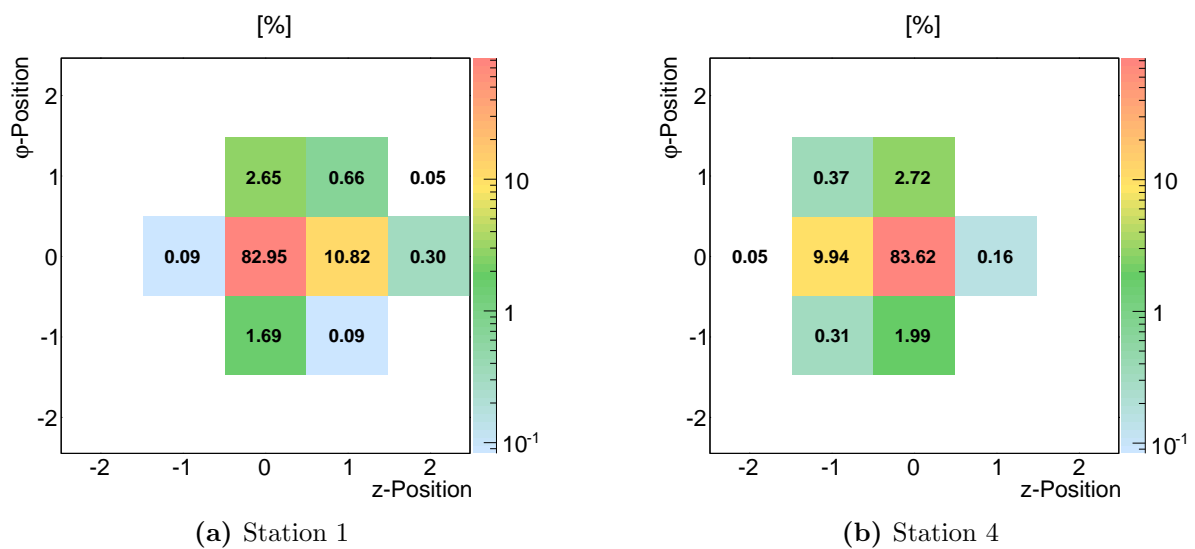
(b) Station 4

Figure B.1.: True tile of first impact relative to estimated tile for station 1 and 4 in the phase 2 setting. For more information see section 6.3.
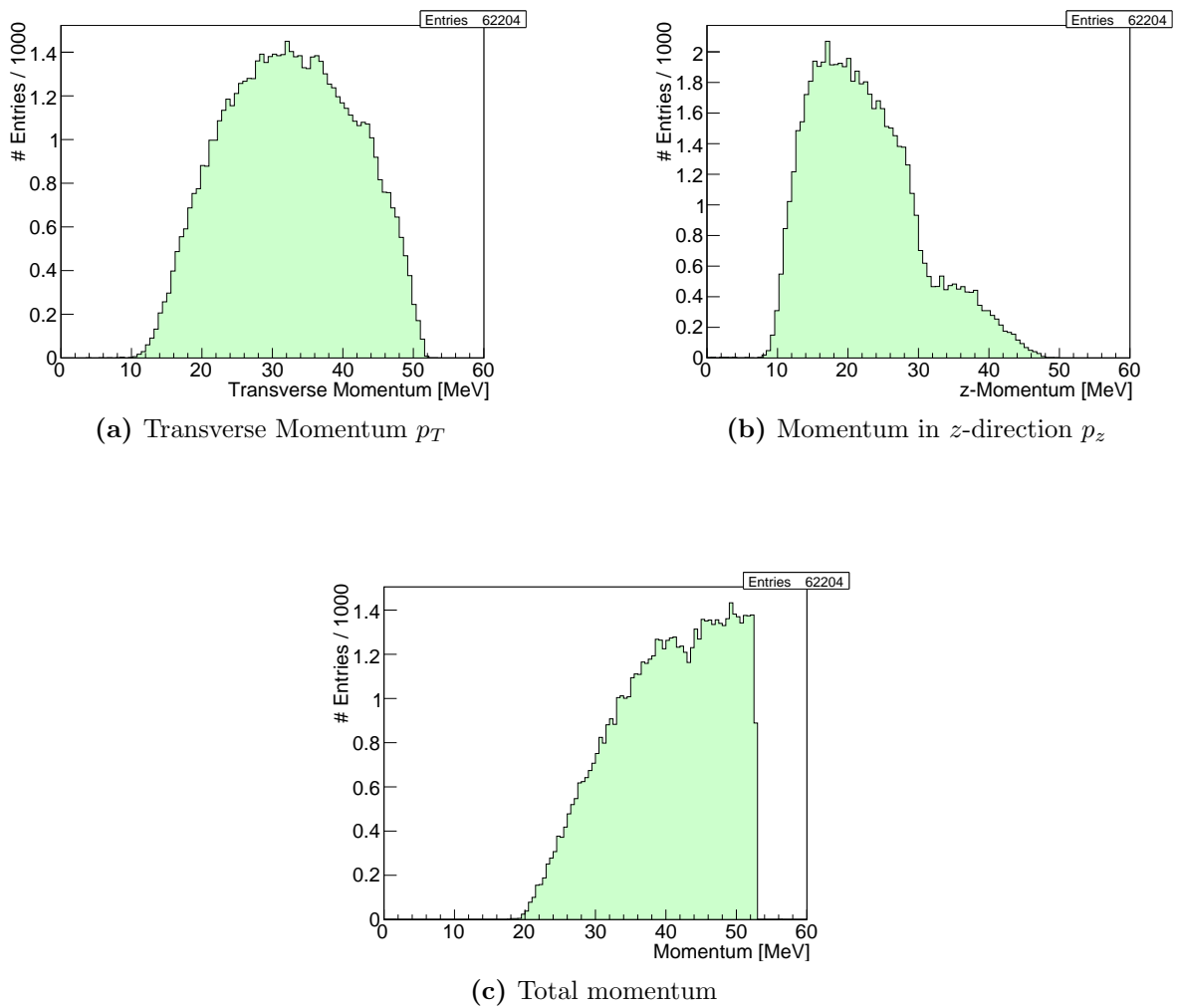
C. Kinematics (Phase 2)

(a) Transverse Momentum p_T

(b) Momentum in z-direction p_z

(c) Total momentum

Figure C.1.: Momentum distribution for reconstructed tracks that hit the tile detector. Shown is **(a)** the transverse momentum, **(b)** the momentum in z-direction, and **(c)** the total momentum. The small dip in the total momentum spectrum is due to the gap between the stations. For Phase 2. For more details see section 5.4

Bibliography

[1] Georges Aad et al. Observation of a new particle in the search for the Standard Model Higgs boson with the ATLAS detector at the LHC. *Phys.Lett.*, B716:1–29, 2012.

[2] Serguei Chatrchyan et al. Observation of a new boson at a mass of 125 GeV with the CMS experiment at the LHC. *Phys.Lett.*, B716:30–61, 2012.

[3] Steven Weinberg. A Model of Leptons. *Phys.Rev.Lett.*, 19:1264–1266, 1967.

[4] Makoto Kobayashi and Toshihide Maskawa. Cp-violation in the renormalizable theory of weak interaction. *Progress of Theoretical Physics*, 49(2):652–657, 1973.

[5] P.W. Higgs. Broken symmetries, massless particles and gauge fields. *Physics Letters*, 12(2):132 – 133, 1964.

[6] François Englert and Robert Brout. Broken symmetry and the mass of gauge vector mesons. *Physical Review Letters*, 13(9):321–323, 1964.

[7] S. W. Herb et al. Observation of a dimuon resonance at 9.5 gev in 400-gev proton-nucleus collisions. *Phys. Rev. Lett.*, 39:252–255, Aug 1977.

[8] G. Arnison et al. Experimental observation of lepton pairs of invariant mass around 95 gev/c2 at the CERN SPS collider. *Physics Letters B*, 126(5):398 – 410, 1983.

[9] Yoshitaka Kuno and Yasuhiro Okada. Muon decay and physics beyond the standard model. *Rev.Mod.Phys.*, 73:151–202, 2001.

[10] Andrew Purcell. Go on a particle quest at the first cern hackfest. http://www.isgtw.org/spotlight/go-particle-quest-first-cern-hackfest, August 2012.

[11] K.A. Olive et al. (Particle Data Group). Particle listings: Muon. *Chin. Phys. C38, 090001*, 2014.

[12] K.A. Olive et al. (Particle Data Group). Particle listings: Electron. *Chin. Phys. C38, 090001*, 2014.

[13] Patrick Eckert. *The Mu3e Tile Detector*. PhD thesis, University of Heidelberg, 2015.

[14] S. Amoruso et al. Measurement of the mu decay spectrum with the ICARUS liquid argon TPC. *Eur.Phys.J.*, C33:233–241, 2004.

[15] DV Forero, M Tortola, and JWF Valle. Global status of neutrino oscillation parameters after neutrino-2012. *Physical Review D*, 86(7):073012, 2012.

[16] Robert H. Bernstein and Peter S. Cooper. Charged Lepton Flavor Violation: An Experimenter's Guide. *Phys.Rept.*, 532:27–64, 2013.

[17] Blondel et al. Research proposal for an experiment to search for the decay $\mu \to eee$. arXiv:1301.6113v1, January 2013.

[18] S. Mihara. MEG experiment at the paul scherrer institute. *Nuclear Physics A*, 844(1–4):150c – 154c, 2010. Proceedings of the 4th International Symposium on Symmetries in Subatomic Physics.

[19] J. Adam et al. New limit on the lepton-flavour violating decay $\mu^+ \to e^+\gamma$. *Phys.Rev.Lett.*, 107:171801, 2011.

[20] K. Hayasaka et al. New search for $\tau \to \mu\gamma$ and $tau \to e\gamma$ decays at Belle. *Phys.Lett.*, B666:16–22, 2008.

[21] J.P. Lees et al. Limits on tau Lepton-Flavor Violating Decays in three charged leptons. *Phys.Rev.*, D81:111101, 2010.

[22] W. Bertl et al. A search for $\mu - e$ conversion in muonic gold. *The European Physical Journal C - Particles and Fields*, 47(2):337–346, 2006.

[23] U. Bellgardt et al. Search for the decay $\mu^+ \to e^+e^+e^-$. *Nuclear Physics B*, 299(1):1 – 6, 1988.

[24] William J. Marciano et al. Charged lepton flavor violation experiments. *Annual Review of Nuclear and Particle Science*, Vol. 58: 315-341, 2008.

[25] Ivan Perić. A novel monolithic pixelated particle detector implemented in high-voltage CMOS technology. *Nuclear Instruments and Methods in Physics Research Section A: Accelerators, Spectrometers, Detectors and Associated Equipment*, 582(3):876 – 885, 2007. VERTEX 2006 Proceedings of the 15th International Workshop on Vertex Detectors.

[26] S. Agostinelli et. al. Geant4—a simulation toolkit. *Nuclear Instruments and Methods in Physics Research Section A: Accelerators, Spectrometers, Detectors and Associated Equipment*, 506(3):250 – 303, 2003.

[27] A. Schöning. A 3d multiple scattering fit for track reconstruction. Talk given at the Mu3e Collaboration Meeting, Internal Note Physikalisches Institut, Heidelberg, October 2012.

[28] J. Beringer et. al. Particle Detectors at Accerlerators. *PR, D86*, 2013.

[29] Saint Gobain. *BC-418 Data Sheet.*

[30] P Buzhan, B Dolgoshein, A Ilyin, V Kantserov, V Kaplin, A Karakash, A Pleshko, E Popova, S Smirnov, Yu Volkov, et al. An advanced study of silicon photomultiplier. *ICFA Inst. Bull*, 21:28, 2001.

[31] Martin Göttlich, Erika Garutti, Alexander Tadday, and Hans-Christian Schultz-Coulon. Application of silicon photomultipliers to calorimetry and positron emission tomography. In *International Workshop on New Photon Detectors PD09*, 2009.

[32] Hamamatsu Photonics. MPPC, Technical Information. *www.hamamatsu.com*, 2015.

[33] D Renker and E Lorenz. Advances in solid state photon detectors. *Journal of Instrumentation*, 4(04):P04004, 2009.

[34] Slawomir S. Piatek. Physics and Operation of an MPPC. *www.hamamatsu.com*, 2014.

[35] Wei Shen, Konrad Briggl, Huangshan Chen, Peter Fischer, Alejandro Gil, Tobias Harion, Michael Ritzert, and H-C Schultz-Coulon. Stic-a mixed mode chip for sipm tof applications. In *Nuclear Science Symposium and Medical Imaging Conference (NSS/MIC), 2012 IEEE*, pages 877–881. IEEE, 2012.

[36] Wei Shen, K. Briggl, Huangshan Chen, P. Fischer, A. Gil, T. Harion, V. Kiworra, M. Ritzert, H.-C. Schultz-Coulon, and V. Stankova. Stic2 - characterization results of a sipm readout asic for time-of-flight applications. In *Nuclear Science Symposium and Medical Imaging Conference (NSS/MIC), 2013 IEEE*, pages 1–5, Oct 2013.

[37] Huangshan Chen et. al. A Dedicated Readout ASIC for Time-of-Flight Positron Emission Tomography using Silicon Photomultiplier (SiPM). 2014.

[38] Wei Shen. *Development of High Performance Readout ASICs for Silicon Photomultipliers (SIPMs)*. PhD thesis, University of Heidelberg, 2012.

[39] H. Spieler. *Semiconductor Detector Physics.* Oxford University Press, 2008.

[40] Alexander Tadday. *Scintillation Light Detection and Application of Silicon Photomultipliers in Imaging Calorimetry and Positron Emission Tomography.* PhD thesis, University of Heidelberg, 2011.

[41] Moritz Kiehn. *watson-package.* Internal package for helix geometry.

[42] Rashid M Djilkibaev and Rostislav V Konoplich. Rare muon decay $\mu^+ \to e^+ e^- e^+ \nu_e \bar{\nu}_\mu$. *Physical Review D*, 79(7):073004, 2009.

[43] HJ Bhabha. The scattering of positrons by electrons with exchange on dirac's theory of the positron. *Proceedings of the Royal Society of London Series A: Mathematical, Physical & Engineering Sciences*, 154(881):195–206, 1936.

[44] Niklaus Berger. Accidental background studies. Internal Note, 2015.

[45] S. Fukui et al. A study on the structure of the extensive air shower. *Supplement of the Progress of theoretical physics*, pages 1–53, 1960.

[46] CP Woidneck and E Bohm. The longitudinal particle distribution in the extensive air shower disc. *Journal of Physics A: Mathematical and General*, 8(6):997, 1975.

Acknowledgements

Erklärung:

Ich versichere, dass ich diese Arbeit selbstständig verfasst habe und keine anderen als die angegebenen Quellen und Hilfsmittel benutzt habe.

Heidelberg, den (Datum)   . . . .